Structure of PAMAM Dendrimers: Generations 1 through 11

Prabal K. Maiti,[†] Tahir Çağın, Guofeng Wang, and William A. Goddard, III*

Materials and Process Simulation Center, Beckman Institute, Division of Chemistry and Chemical Engineering, California Institute of Technology, Pasadena, California 91125

Received October 29, 2003; Revised Manuscript Received April 22, 2004

ABSTRACT: The structure and dynamics of poly(amido amide) (PAMAM) dendrimers have been of great interest both scientifically and industrially, but such important features as the distributions of atoms, channels, and strain inside these molecules remain unresolved. This paper reports results from systematic investigations of the atomistic structure of ethylenediamine (EDA) cored PAMAM dendrimer up through the 11th generation (294 852 atoms), at which point the strain energy has risen to a point that limits uniform growth of additional layers. Here we report, as a function of generation, structural properties such as radius of gyration, shape tensor, asphericity, fractal dimension, monomer density distribution, solvent accessible surface area, molecular volume, and end group distribution functions, all evaluated from extensive molecular dynamics (MD) at 300 K. We find that the radius of gyration scales as $R_g \sim N^{1/3}$ over the entire range of generations, suggesting rather uniform space filling for all generations. Contrary to common expectation, we find that the outer subgenerations penetrate substantially into the interior of the dendrimer, even for G11. Consequently, the terminal amine groups are distributed throughout the interior, not just on the periphery of the dendrimer. However for G6 through G11 there is a large region of uniform density, supporting the uniform scattering model often used in interpreting the SANS (small-angle neutron scattering) and SAXS (small-angle X-ray scattering) data, which lead to sizes in excellent agreement with the calculations. The calculated single particle form factor approaches that of a sphere as the generation number increases. For the larger generations, we found that the use of continuous configuration biased Monte Carlo (CCBB MC) was essential to construct initial configurations that lead to lower final strain energies.

1. Introduction

Dendritic polymers or dendrimers are synthesized using a stepwise repetitive reaction sequence that guarantees a very highly monodisperse polymer,[1] with a nearly perfect hyperbranched topology radiating from a central core and grown generation by generation. The synthetic procedures developed for dendrimer preparation permit nearly complete control over the critical molecular design parameters, such as size, shape, surface/interior chemistry, flexibility, and topology. Synthetic techniques proved effective in generating macromolecules with a unique combination of properties include the Starburst divergent strategy,[2−4] the convergent growth strategy,[5−8] and the self-assembly strategy.[9]

The atomistic characterization of dendrimer structure has lagged behind this rapid progress in synthesis and design.[1] The problem is that these molecules possess an enormous number of energetically permissible conformations, and in solution, there is rapid interchange between them. Thus, diffraction techniques yield little structural information. Also many generations involve the same monomers, making it difficult to extract precise information about the local structure from infrared or NMR experiments. Thus, the first precise experimental data about the gross size came from size exclusion chromatography (SEC), which is now being complemented with small-angle neutron scattering (SANS) and small-angle X-ray scattering (SAXS) to determine the gross size and some structural details of dendrimers.[10−12]

The structural aspects of dendrimers became a lively area of research interest at the Winter Polymer Gordon Conference in 1983 at which D. Tomalia first described the synthesis of PAMAM dendrimers. This led to the paper describing the dendrimer surface-congestion property now referred to as the de Gennes dense packing phenomenon.[13] This was followed by the first molecular level modeling studies by Goddard and co-workers[1,14] of the structural properties of NH_3-cored poly(amidoamine) (PAMAM) dendrimers (up to generation 6) and polyether dendrimers (up to the self-limiting generation 4).

PAMAM dendrimers have led to applications ranging from drug delivery to molecular encapsulation and gene therapy, from building blocks for nanostructures to micelle mimics as decontaminating agents.[15] For these materials to be of maximum use for such diverse application, it is essential to obtain a comprehensive understanding of their structure and dynamics. Properties such as the shape and size of the dendrimers as a function of generation, solvent accessible surface area, monomer distribution, and distribution of terminal groups are all critical for some applications of dendrimers. Since the early modeling studies,[1,14,16] a number of theoretical and computer simulation studies have been reported on structural properties of dendrimer under various conditions.[17−27] However, many studies have focused on simple bead models of dendrimers to obtain qualitative features, or the molecular level simulations have been performed only for the lower generations. These studies have provided increased insight into some structural and dynamical properties of dendrimer systems, but there remain controversies regarding the distribution of the terminal end groups within the dendrimers and their location on the periphery of the

* To whom all correspondence to be addressed. E-mail: wag@wag.caltech.edu.
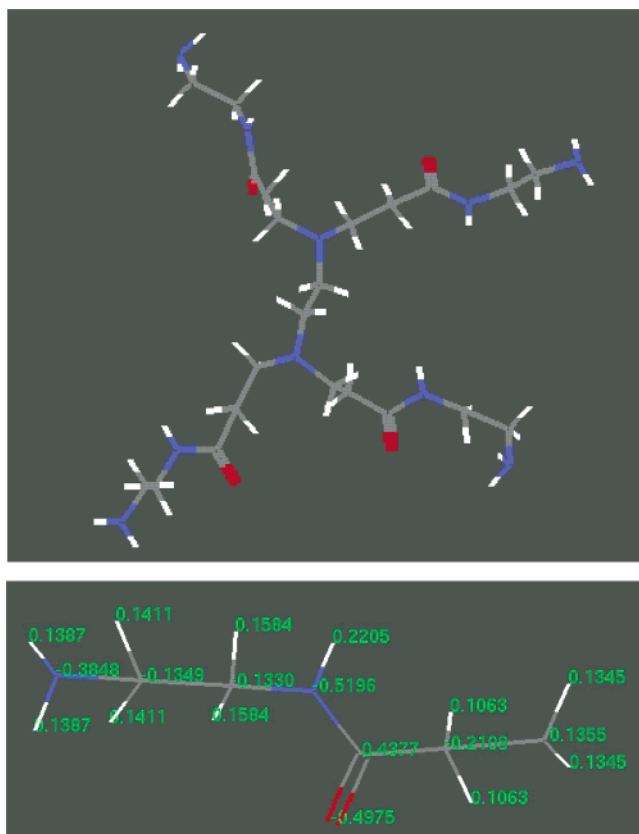† Present address: Department of Physics, Indian Institute of Science, Bangalore, India 560012.

Figure 1. (a) Chemical structure of the EDA-cored PAMAM dendrimer for generation 0 and (b) the repeat unit. The partial charges on each atom are also displayed. Here, the blue atoms are nitrogen, the red atoms are oxygen, the white atoms are hydrogen and the gray atoms are carbon.

Table 1. Number of Atoms, and Terminal Nitrogen for Fully Atomistic Model of PAMAM Dendrimer for G0 to G11

generation	no. of atoms	terminal nitrogens	generation	no. of atoms	terminal nitrogens
0	84	4	6	9156	256
1	228	8	7	18 372	512
2	516	16	8	36 804	1024
3	1092	32	9	73 668	2048
4	2244	64	10	147 396	4096
5	4548	128	11	294 852	8192

molecule. Furthermore, neither the atomistic level nor the bead-model simulations have yet investigated the limiting generation issue, which was first raised by de Gennes.

To provide a detailed and consistent understanding of the structures and properties of PAMAM polymers from generation 0 to generation 11, we carried out a systematic series of fully atomistic simulation on all generations up to the limiting generation, which we find to be G11. The calculations are all based on the ethylenediamine (EDA) core and the PAMAM monomer shown in Figure 1.

To reliably resolve such issues requires application of a fully atomistic description of dendrimers. Because of the geometric growth in the number of monomers (or number of atoms) with generation number (Table 1), leading to 294 852 atoms for G11, and because of the topological constraints imposed by the core and monomer functionality (number of branch points), it is essential to construct the three-dimensional structures systematically so that comparisons can be made be-

tween various generations. Because of the topologically constrained nature of the dendrimers for higher generations, neither molecular dynamics (MD) nor Monte Carlo (MC) techniques suffice to explore the configurational space far from the initial structures. Consequently, we used the continuous configurational Boltzmann biased (CCBB) direct Monte Carlo (MC) method[28,29] to construct fully atomistic, energetically permissible, and highly probable initial configurations for different generations of PAMAM dendrimers. After constructing these initial configurations with MC, we employ MD simulations first to anneal the structures and then to collect the equilibrium data at the constant temperature conditions to extract the properties of these dendrimers.

Essentially all experiments on the structures and properties of PAMAM dendrimers have been for solution phase, usually aqueous. However, the exponential growth in the number of monomers with the generation number makes the study the structure and dynamics of all structures up to the self-limiting point (G11 with ~300 000 atoms) a formidable task even for the gas phase. Indeed such studies of the structure and dynamics of PAMAM dendrimer up to the limiting generation have not been reported previously either in the gas phase or in the presence of solvent. Thus, since our goal in this paper is to characterize the properties for generations up to the limiting growth size, we consider only the gas phase in the present study. The properties obtained here for the gas phase should mimic the behavior of the system in the presence of poor solvent, providing valuable information about the behavior of PAMAM systems in such solvents. The current results will be compared to similar simulations of these system in aqueous solution in a future publication,[30] albeit for up to G6, much smaller than the self-limiting generation. The current gas phase results will provide the basis for systematically extracting the effect of solvent on the structure and dynamics of PAMAM dendrimers. In addition we are using these fully atomistic studies to provide the basis for deriving the effective interaction parameters for coarse-grained descriptions of PAMAM dendrimers, which will dramatically reduce the number of degrees of freedom in the system allowing the study of structure and dynamics over longer time scale. Our preliminary results [31] on such a coarse-grained model shows excellent agreement with this fully atomistic simulation results up to the limiting generations.

2. Model Systems Constructions and Method Used in Simulations

We generated the initial 3-dimensional structures of PAMAM dendrimers up to generation 11 using the CCBB MC method.[28,29] These CCBB generated structures were subsequently subjected to conjugate gradient minimization (to an RMS force of 0.1 (kcal/mol)/A) to further improve the starting configurations. We further annealed these minimized structures using NVT MD (Nose-Hoover thermostat with damping constant of 0.1 ps) at a variety of temperatures and finally cooled to 300 K to obtain the initial equilibrated configurations. These MD simulations used a time step of 0.001 ps and the anneal cycle was typically as follows. The initial minimized structure was heated at a rate of 100 K/4 ps from 300 to 2000 K, followed by quenching to 1000 K at the same rate, followed by four such cycles between 1000 and 2000 K, and finally cooling to 300 K. In the following, we briefly describe the CCBB method.

2.1. CCBB Method and Construction of Dendrimers. To predict the polymer properties of such complex polymers as PAMAM, we need to determine an ensemble of conformations that would be highly populated at the temperature and pressure of interest. To accomplish this task, we use continuous configurational biased (CCB) direct Monte Carlo sampling[28,29] in which each torsion in the polymer chains is sampled using a weighting function based on the Boltzmann factor of the torsion energy plus nonbonding interactions in the vicinity of the growing chain end (within a cutoff sphere of radius R_C)

$$W_{CCB}(\phi_i;\phi_1,...,\phi_{i-1}) = \frac{g_{CCB}(\phi_i;\phi_1,...,\phi_{i-1})}{z_{CCB}(\phi_1,...,\phi_{i-1})} \quad (1)$$

where

$$z_{CCB}(\phi_1,...,\phi_{i-1}) = \int_0^{2\pi} g_{CCB}(\phi_i;\phi_1,...,\phi_{i-1})\,d\phi_i \quad (2)$$

$$g_{CCB}(\phi_i;\phi_1,...,\phi_{i-1}) = g_{IRS}(\phi_i)\exp[-\beta\sum_{j,k}\Theta(R_C - r_{jk})E_{LJ}(r_{jk})] \quad (3)$$

Here atom j belongs to the growing chain end group and atom k is one of the atoms in the grown polymer chains. And $\Theta(R)$ is the Heaviside step function, namely $\Theta(R) = 0$ when $R < 0$ and $\Theta(R) = 1$ when $R \geq 0$.

Prior to each step of chain sampling, the torsion energy and nonbonding energy within the cutoff radius of the growing end were calculated for 200 grid points equally separated from 0 to 2π, and W_{CCB} was evaluated. A random number, ξ, uniformly distributed in the interval (0,1), was drawn and the torsion angle is obtained by requiring

$$P_{CCB}(\phi_i) = \int_0^\phi W_{CCB}(\phi)\,d\phi \quad (4)$$

We applied this algorithm to construct the initial dendrimer structures such as assemblies of spherical and cylindrical giant liquid crystalline structure of Percec and co-workers [32-34] and various other polymers.[35-38] All of the initial configurations for PAMAM dendrimers from generations 1 through 11 were obtained by CCBB method.

2.2. Force Fields and Simulation Methods. We carried out MD simulations at room temperature for generation 1 through 11. These simulations employed the Dreiding force field[39] to describe the interatomic interactions. The partial charges on the atoms are derived using the charge equilibration (QEq) method, as follows.[40] First we evaluated the QEq charges for the core, as a neutral molecule using generation 0, i.e., with all four terminal H atoms replaced by four monomers of the PAMAM dendrimer. Then, we evaluated the QEq charges for the full monomer of PAMAM, where all three H atoms are replaced by three monomers of PAMAM, with the required charge neutrality. Finally we evaluated the QEq charges for the terminal PAMAM monomers; where the two terminal H atoms are kept as H and the other H is replaced by a monomer of the PAMAM dendrimer. These charges for the terminal PAMAM monomer were then scaled to be neutral and were used for the terminal generation. This procedure ensures that each generation is neutral. Figure 1 shows the partial charges derived from QEq for the various
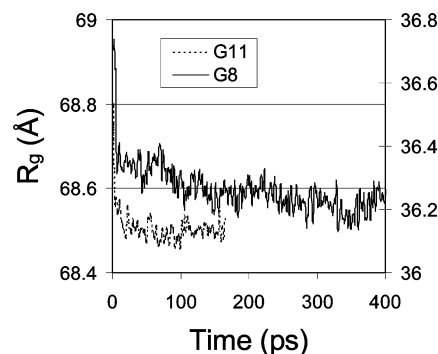

Figure 2. Time evolution of the radius of gyration (R_g) of the PAMAM dendrimers, generation 8 (400 ps) and generation 11 (180 ps), during simulation.

atom types for the full monomer of PAMAM. All simulations treat the terminal nitrogens as having two H's, which is appropriate for the gas phase. In another paper, we will consider explicit solvent and the possibility of protonated primary and secondary amines.[30]

To evaluate the nonbonded coulomb and van der Waals interactions, we employed the cell multipole method (CMM),[41] which includes the interactions with all atoms (no cutoffs), using multipole expansions. These calculations used up to quadruple expansions in the far field and local potential. The bounding box was adjusted to have an average of 6−10 particles per leaf cell.

All calculations reported here were carried out with the MPSim program.[42] Molecular dynamics simulations employed an integration step of 1 fs to maintain conservation of Hamiltonian. The simulations were conducted at $T = 300$ K, and for generations 3−8 we used 200 ps for equilibration and 200 ps for the data collection. For generations 9−11 we used 50 ps for equilibration and 50−100 ps for the data collection. The equilibration process was monitored by measuring the total energy as well as the instantaneous radius of gyration of the dendrimer. As shown in Figure 2, for the variation of the radius of gyration as a function of time for generation 8 (400 ps) and generation 11 (180 ps), the simulations are long enough to obtain reliable structural and thermodynamic properties. Furthermore, for higher generations, the branched topology of the dendrimers inhibits major conformational excursions that might be observed in linear polymers in long time simulations; thus, the length of simulations used in this study is long enough to determine physical and structural properties of high generation dendrimers. This is further confirmed from our longer molecular dynamics simulations of the atomistically informed two bead-per monomer coarse-grained model.[31] We saved the configurations at 0.5 ps interval and used these configurations to determine the average properties at $T = 300$ K. The next section presents the simulation results.

To ensure that we have generated equilibrated structures we did the following computer experiments: we took the final equilibrated G10 PAMAM structure and made it the G9 dendrimer by removing the outer generation. Molecular dynamics was continued on this new and independent G9 PAMAM dendrimer and within 50 ps, the radius of gyration converged to $R_g = 45.24$ Å, which is within 2% of the previously obtained value, $R_g = 46.03$ Å.
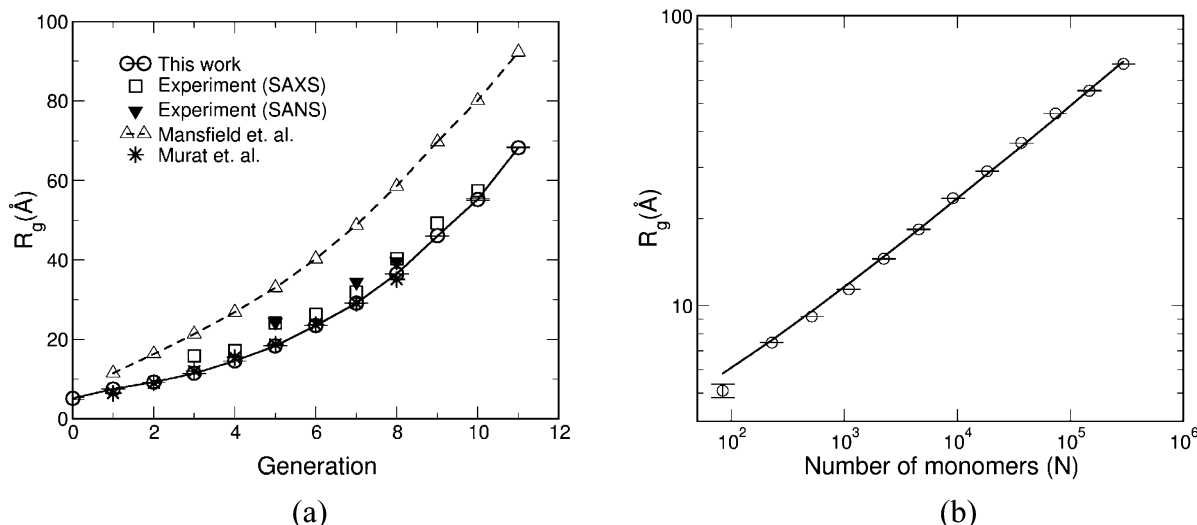
(a)   (b)

Figure 3. (a) Average radius of gyration R_g of dendrimers as a function of generation. Our values were averaged from the snapshots every 0.5 ps from the equilibrium molecular dynamics trajectory (i.e., after the equilibration run). The data obtained from SAXS and SANS experiments are also shown. Also included are the results from the MC simulation of dendrimers on a diamond lattice by Mansfield and Jeong (ref 20) and from the Brownian Dynamics simulations of Murat et al. (ref 26). Both Mansfield's and Murat et al. data have been scaled by the average bond length, $\langle b \rangle = 1.5$ Å, to obtain distances in Å. (b) A log–log plot of calculated R_g from our simulations as a function of the number of atoms (N) in the dendrimer. The solid line shows the fit, $R_g = 1.34 + 1.026 N^{0.33}$.

3. Results

To characterize the structure and properties of these EDA-cored PAMAM dendrimers as a function generation, we have chosen the following quantities:
- Radius of gyration.
- Shape tensor.
- Asphericity.
- Monomer density distribution.
- Spatial arrangement of branch points.
- Terminal group distribution.
- Energy per monomer.
- Molecular surface area.
- Solvent accessible surface area.
- Molecular volumes as a function of generation.
- The fractal dimension.

3.1. Size. The mean-square radius of gyration $\langle R_g^2 \rangle$ provides a quantitative characterization of the dendrimer size and the shape is characterized by the shape tensor of the individual chains. For a dendrimer with N atoms the mean-square radius of gyration is given by

$$\langle R_g^2 \rangle = (1/M) \langle [\sum_{i=1}^{N} m_i |r_i - R|^2] \rangle \qquad (5)$$

where R is the center-of-mass of the dendrimer, m_i is the mass of the ith atom, and M is the total mass of the dendrimer. Figure 3a and Table 2 show the radius of gyration R_g as a function of generation. Here, we see good agreement between our calculated R_g with those obtained form the recent small-angle neutron scattering (SANS) and small-angle X-ray scattering (SAXS experiments. Table 2 allows a more detailed comparison of the R_g from our simulations with experiment. We see that for lower generations (3–6) the calculated R_g is considerably smaller than the experimental values (20–30%). However, for larger generations R_g approaches experimental numbers, for generations 7 and 8 the difference is around 10% for G9–G11 the difference is about 5%. This discrepancy is probably because in the difference in conditions. Thus, most experiments on

Table 2. Radius of Gyration (R_g) (Å) as a Function of Generation for PAMAM, Where R_N Is the Radius of Gyration Considering Only the Terminal Nitrogens[a]

| generation | this work | | experiment | | Mansfield | | Murat |
	R_g	R_N	SAXS	SANS	R_g	R_N	R_g
0	4.93	6.80					
1	7.46	10.36			7.63	8.64	4.27
2	9.17	11.61			10.88	12.44	6.01
3	11.23	12.91	15.8		14.2	16.05	7.96
4	14.5	16.81	17.1		17.87	19.86	10.27
5	18.34	20.26	24.1	24.3	21.99	24.00	12.49
6	22.4	24.67	26.3		26.82	28.8	15.79
7	29.09	31.55	31.9	34.4	32.48	34.39	19.37
8	36.42	39.87	40.3	39.5	39.04	40.88	20.41
9	46.03	47.94	49.2		46.47	48.28	
10	55.19	57.38	57.4		53.42	55.28	
11	68.25	70.86			61.51	63.60	

[a] Our values were averaged from snapshots every 0.5 ps in the dynamics (after equilibration). Small-angle X-ray scattering (SAXS) results are from ref 61. Small-angle neutron scattering (SANS) results for generation 5 and 8 are from ref 11 and for generation 7 are from ref 56. Mansfield and Jeong[20] used Monte Carlo simulations on a diamond lattice dendrimer model described by seven step spacers using spacers of step size $b = 3^{1/2}$. Murat et al.[26] used Brownian dynamics simulations on a bead model dendrimers with seven step spacers with average bond length $b = 0.97$.

PAMAM dendrimers have been performed in polar solvents with terminal groups protonated in the presence of counterions. In these circumstances, the hydrophilic nature of the primary and tertiary amines leads to a substantial swelling in PAMAM dendrimers. For larger generations (beyond $G = 8$), we expect that the more rigid nature of the dendrimer framework moderates the role of solvent and degree of protonation in affecting the conformation and size of the dendrimer.[11,43,44] Presumably this is why we find better agreement in R_g for higher generations. Thus, we interpret our calculations with neutral dendrimers in terms of nonpolar poor solvent conditions (i.e., gas phase). Preliminary computations using explicit polar solvents (water) for generation 6 show a substantial (15%) increase in radius leading to a value of $R_g = 26.76$ Å,
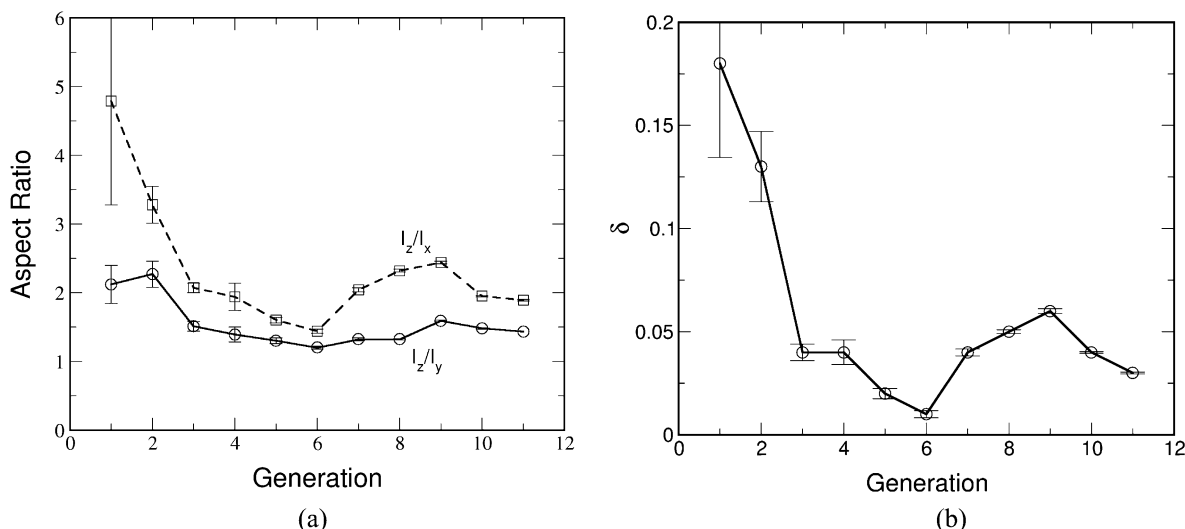
Figure 4. (a) Moment of inertia based aspect ratios as a function of generation ($I_z > I_y > I_x$) and (b) the asphericity parameter, δ, as a function of generation. The values plotted were averaged using the snapshots every 0.5 ps from the equilibrium molecular dynamics trajectory. The solid line is only to guide the eye.

while the protonated model systems lead to an even larger effect (20%).[30] MC simulations of G5 dendrimer by Welch and Muthukumar [18] predicted that depending on the solution pH and salt concentration the size of the dendrimer can change by up to a factor of 1.8!

Figure 3b shows for G3 to G11 the sizes scale as $R_g \sim N^{1/3}$, indicating that these PAMAM dendrimers all have a homogeneous structure in which the atoms are densely packed. A recent SANS study on poly(benzyl ether) dendrimers [45] finds that the size of the dendritic molecules increase as $M^{0.32}$, where M is the molecular weight of the molecules. This is in good agreement with our calculations, indicating the very compact structure expected in a poor solvent.

The scaling exponent calculated here agrees well with the molecular dynamics simulation with stochastic terms including some friction on a bead model by Murat and Grest,[26] whose data have been scaled by $b = 1.5$ Å (average bond length) to obtain distances. This compact structure requires a space filling geometry that implies considerable back-folding of the outer generations. Indeed, this back-folding is evident from several lines of evidence as will be discussed below.

3.2 Shapes of Dendrimers. The size and shape of the dendrimer have been measured using transmission electron microscopy (TEM)[46] and with tapping mode atomic force microscopy (AFM).[47] In the TEM images the dendrimer molecules appear as dark objects on a light background of the amorphous substrate, and they are well separated from each other. This helps in accurately measuring the size and shape. TEM studies indicate that higher generations dendrimer (G7−G10) are spherical in shape, with some molecules showing "edges" or slightly polyhedral shape. The shape and size of the G10 dendrimer was studied also by Cryo-TEM methods.[46] The Cryo-TEM images of G10 indicate it to be of a more polyhedral or irregular shapes than those observed in the TEM images. The projected shapes of the dendrimer also do not appear circular. This led the authors[46] to conclude that since the dendrimers are synthesized from the EDA core, they might retain the tetrahedral shape of the core molecule.

AFM images were used to study the shape and size of the generation 5−10 PAMAM dendrimers. For lower generations (G5 and G6) the shapes in the TEM images become less distinct. AFM images of the dendrimers on mica surface[47] indicate that molecules are dome-shaped instead of being spherical. These authors suggest that the deformation is caused by the dendrimers spreading out to flatten on the surface. The G4 dendrimer cannot be imaged due to its lower rigidity and smaller number of surface functional groups.

Previous computer simulations by Goddard and co-workers on NH_3 core dendrimers [14] predicted an abrupt change in the shape of the dendrimer molecules in going from lower to higher generations. In particular they found highly asymmetric shapes for generations 1−3 but nearly spherical shapes for generations 5−7, with G4 at a transition between the two forms. This prediction was confirmed by experiments through photochemical and spectroscopic probes by Turro, Tomalia, and co-workers.[48] Recent MD and MC studies on model dendrimers (mostly with a bead representation of monomers) up to generation 6 [21,49] indicate a rather smooth and continuous transition toward spherical shape in going from G1 to G6.

Figure 5 provides an clue to the character by showing a snapshot of the final configuration for each generation G1 to G11. However to provide a more quantitative criteria to help settle these various contradictory findings and speculations, we calculated the shape of the dendrimer for generations 1−11. The shape tensor describing the mass distribution is given by[50]

$$G_{mn} = (1/M)\left[\sum_{i}^{N} m_i(r_{mi} - R_m)(r_{ni} - R_n)\right], m,n = x,y,z \tag{6}$$

The three eigenvalues of $\mathbf{G}$, I_z, I_y, and I_x (in descending order), are the principal moment of the equivalent ellipsoid. The sum of three eigenvalues is an invariant of the shape tensor $\mathbf{G}$, giving $\langle R_g^2 \rangle$. The ratio of these three principal moments is a measure of *eccentricity* (minor−major axes ratio) of the shape ellipsoid of the dendrimer. Rudnick and Gaspari [27] introduced a better definition of *asphericity* frequently used in the literature as

$$\delta = 1 - 3(\langle I_2 \rangle / \langle I_1^2 \rangle) \tag{7}$$

Table 3. Calculated Average Values of the Three Principal Moments of Inertia of Various Generations PAMAM Dendrimers from MD Simulations[a]

generation	I_z	I_y	I_x	(I_z/I_y)	(I_z/I_x)	d
0	13.51 (1.69)	8.01 (0.93)	2.96 (0.68)	1.73 (0.38)	4.92 (1.33)	0.15
1	33.17 (3.14)	15.63 (1.32)	6.92 (1.28)	2.12 (0.28)	4.79 (1.51)	0.18
2	48.18 (2.37)	21.27 (1.17)	14.71 (0.87)	2.27 (0.19)	3.28 (0.27)	0.13
3	59.11 (1.24)	39.04 (1.31)	28.54 (3.86)	1.51 (0.07)	2.07 (0.07)	0.04
4	95.55 (3.60)	68.88 (5.47)	49.13 (2.34)	1.39 (0.11)	1.94 (0.20)	0.04
5	140.66 (2.33)	107.91 (2.08)	87.75 (1.41)	1.30 (0.04)	1.60 (0.04)	0.02
6	198.40 (2.03)	165.51 (1.41)	137.86 (1.48)	1.20 (0.02)	1.44 (0.03)	0.01
7	376.30 (3.91)	285.83 (2.76)	184.29 (1.88)	1.32 (0.02)	2.04 (0.03)	0.04
8	602.31 (3.49)	456.42 (1.32)	259.46 (1.33)	1.32 (0.01)	2.32 (0.02)	0.05
9	1038.82 (4.53)	655.84 (2.82)	423.99 (1.80)	1.59 (0.01)	2.44 (0.02)	0.06
10	1392.63 (3.62)	940.50 (2.10)	713.35 (2.56)	1.48 (0.01)	1.95 (0.01)	0.04
11	2101.52 (13.73)	1469.71 (10.14)	1112.77 (4.78)	1.43 (0.01)	1.89 (0.01)	0.03

[a] $I_z > I_y > I_x$. δ is the asphericity parameter defined in eq 7. The uncertainties over the dynamics are shown in brackets. Our values were averaged from snapshots every 0.5 ps in the dynamics (after equilibration).

where I_i are the respective invariants of the gyration tensor and are given by

$$I_1 = I_x + I_y + I_z, \quad I_2 = I_x I_y + I_y I_z + I_x I_z, \quad \text{and}$$
$$I_3 = I_x I_y I_z$$

The shape of the dendrimer can be assessed from the average values of the ratio of three principal moments of inertia of the molecules. The average values of the three principal moments of inertia are tabulated in Table 3, while Figure 4 shows the average ratios for different generations dendrimer. We see that the aspherical character plummets from G1 to G2 to G3 and that, from G3 to G11, $\delta \sim 0.04$. The instantaneous snapshots (Figure 5) show that their shape does not deviate much from a sphere. These snapshots have been generated using VMD software[51] developed at UIUC.

The asphericity seems to drop monotonically from G4 to G6 and then increase from G7 to G9 and finally go toward $\delta \sim 0$ for G9−G11. Thus, we find the PAMAM dendrimer of generations G4−G6 to be more spherical in shape than the G9−G11. The trend from G9 to G11 could be caused by the dramatically increased strain in those systems (vide infra), but we do not have an explanation for the minimum asphericity of G6.

We see that beyond generation 3, (I_z/I_y) are in the range 1.0−1.6 and (I_z/I_x) are in the range 1.2−2.5. This means that these dendrimer are compact ellipsoids− spheroids in shape. The asphericities of dendrimers shown in Figure 4b also reveal strongly compact spherical structures.

3.3. Radial Monomer Density Profiles. The average radial monomer density $\rho(r)$ can be defined by counting the number $N(r)$ of atoms whose centers of mass are located within the spherical shell of radius r and thickness Δr. Hence, the integration over r yields the total number of monomers as

$$N(r) = 4\pi \int_0^\infty r^2 \rho(r) \, dr \qquad (8)$$

Figure 6 shows the radial monomer density profiles for each generations G1, G5, G9, and G11 (see Supporting Information for other generations). In each case the plot shows the contributions to a particular generation from each of its component generations. In each case, we take the origin as the center of mass.

For G1−G3 the density has a spike at small R and then decreases somewhat monotonically, but for all higher generations, it shows a minimum at the core and gradually increases to have a maximum at a distance that roughly corresponds to its radius of gyration. A region of almost constant density follows this. Monomer density in this constant density regime is increases with the generation. The extent of the constant density zone increases gradually for higher generations. For G6 the width of this constant density zone is only 5 Å, while it becomes ∼50 Å for G11. Beyond the constant density regime is a tail zone where the density decays monotonically. The width of the tail zone is quite similar for the higher generations dendrimer, ∼25−30 Å for G7− G11.

Several features deserve special mention. For G1− G3, we find a local density minimum near core of the molecule, similar to previous findings.[24,26] However, for higher generations, we find that this feature disappears. Our studies as well as others[49] reveal the presence of a plateau (constant density zone) in the monomer density profiles. This contrasts sharply with the results from the self-consistent mean field model of Boris and Rubinstein,[52] which predicts the largest density at the core, followed by a monotonic decay to the edge of the molecule. We suspect that this is a result of not accounting for the local strain in the higher generations.

We find that the core domain is dense for generations up to G7 but that for higher generations it drops dramatically.

A dramatic feature in the simulations is the high degree of back-folding in the partial density profiles for the various subgenerations. The extent of back-folding increases with the increase in generations. For example, up to G9 the outermost subgeneration remains ∼5 Å away from the center of the molecule. But beginning at G10, this outermost subgeneration gradually penetrates to the core. This finding supports the solid-state NMR measurements on flexible dendrimers,[53] which reveal close contact between the core and peripheral groups. Longitudinal NMR relaxation times in paramagnetic core dendrimer [54] also indicated penetration of the various subgenerations close to the core of the molecules. This is in qualitative agreement with other coarse-grained and atomistic simulation studies on dendrimer systems.[54,55]

3.4. Terminal Amine Group Distribution. The rheological properties and surface activities of the PAMAM dendrimers in solution depend strongly on the location of the terminal groups (which may be protonated or charged) and their distribution within the molecule. The early discussions of dendrimers and the usual schematic diagrams convey the idea that the terminal groups are located at the periphery of the molecule. However, we find substantial folding back of
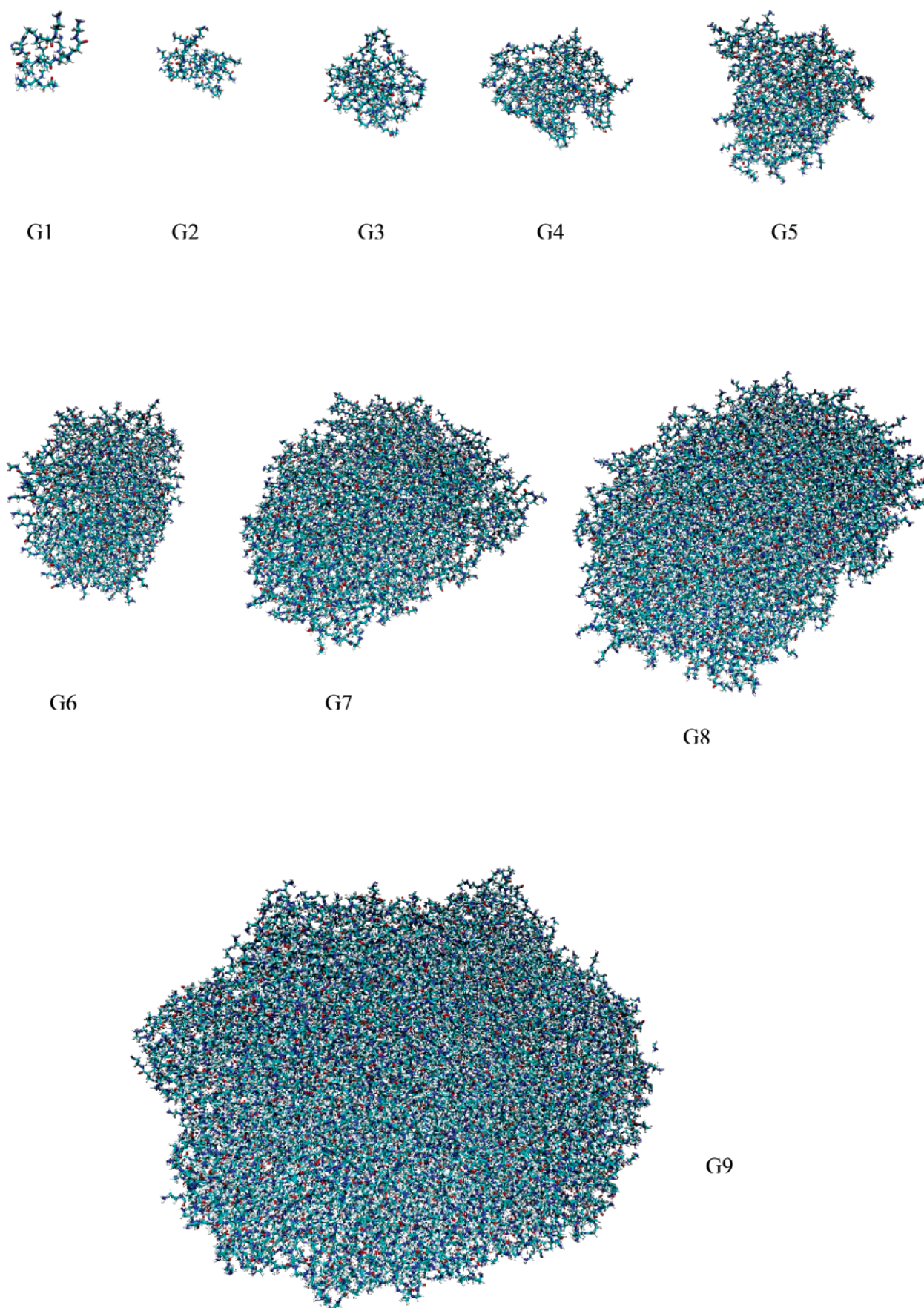
Figure 5. Instantaneous snapshots of G1−G11 PAMAM dendrimers after long MD simulations at $T = 300$ K. All figures are to the same scale. The color-coding of atoms is the same as in Figure 1.
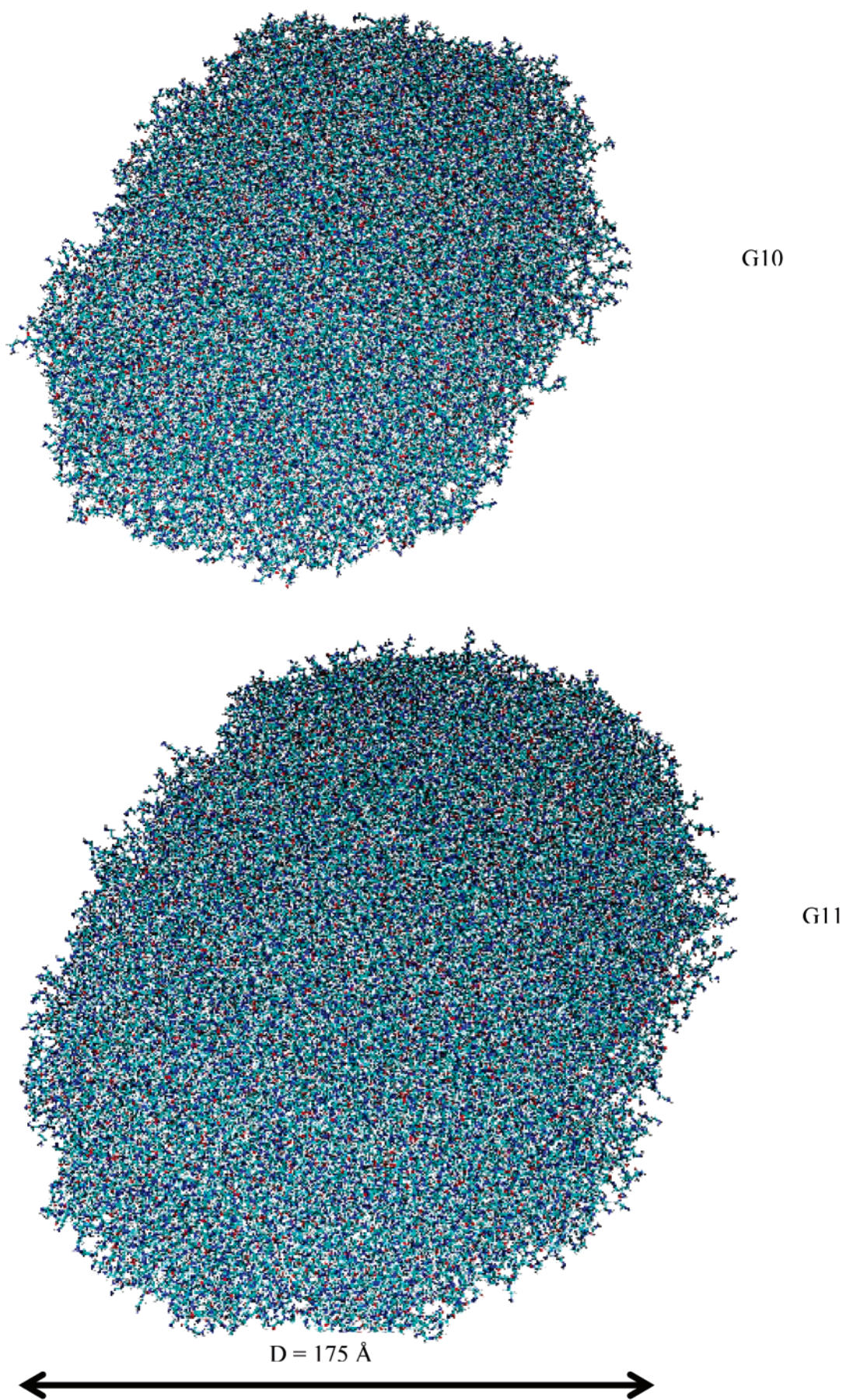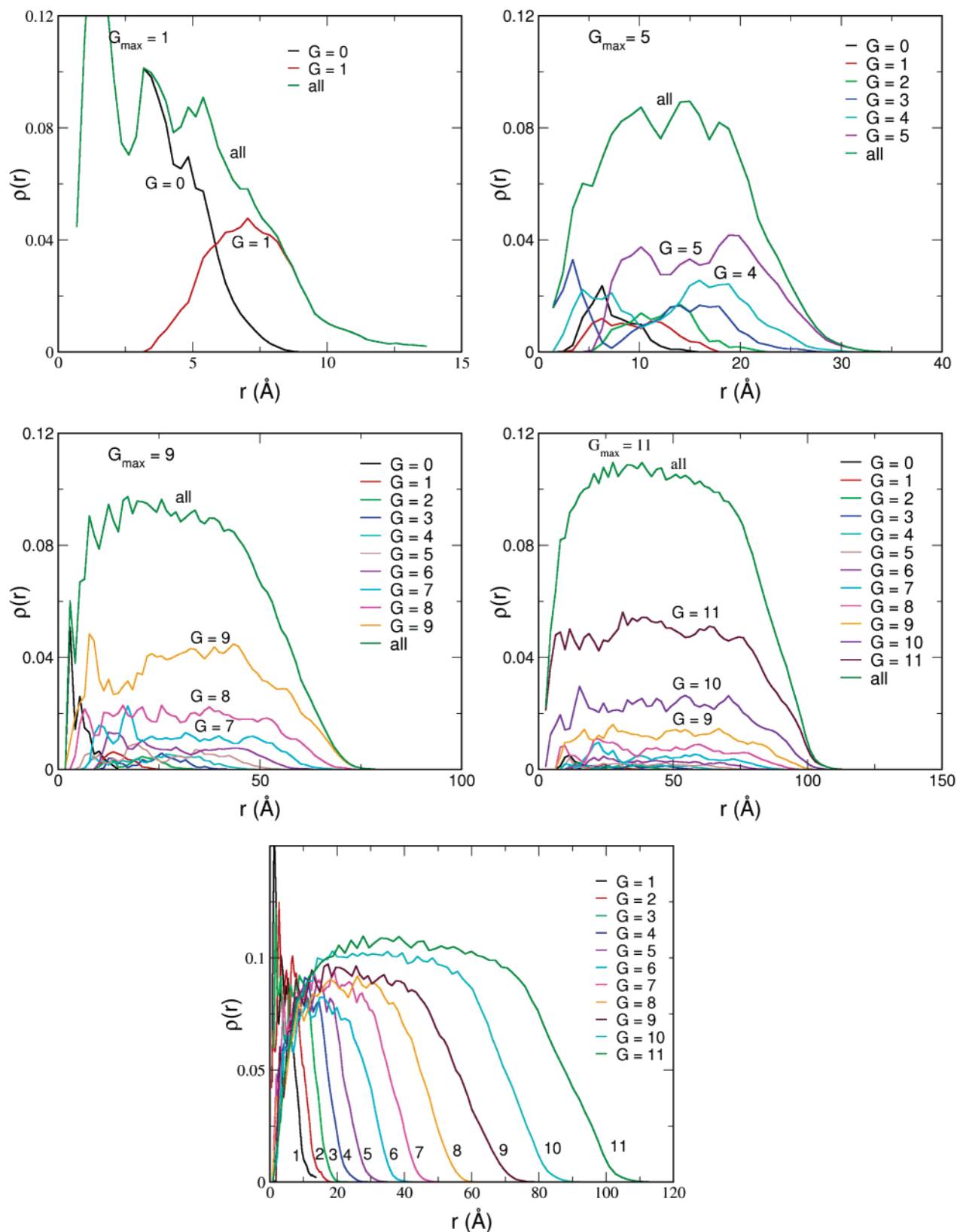
Figure 5. Continued

Figure 6. Radial monomer densities (units gm/cm³) for different generations of EDA-cored PAMAM dendrimers for all generations. Each figure is for a specific generation. The numbers shown were averaged from snapshots every 0.5 ps. The origin is at the center of mass. The last plot compares the total density profiles for all generations of PAMAM dendrimer from G1 to G11.

the end groups inside the dendrimer molecule. To quantify this we show in Figure 7 the density profile for the terminal nitrogens for various generations. This indicates that the end groups of different subgenerations of a given dendrimer are sufficiently flexible to inter-

penetrate nearly the whole molecule. In particular, the end groups of the higher generations even come close to the core of the molecule. This result is in agreement with the theoretical analysis of Boris and Rubinstein[52] as well as other atomistic MD studies on dendrimer
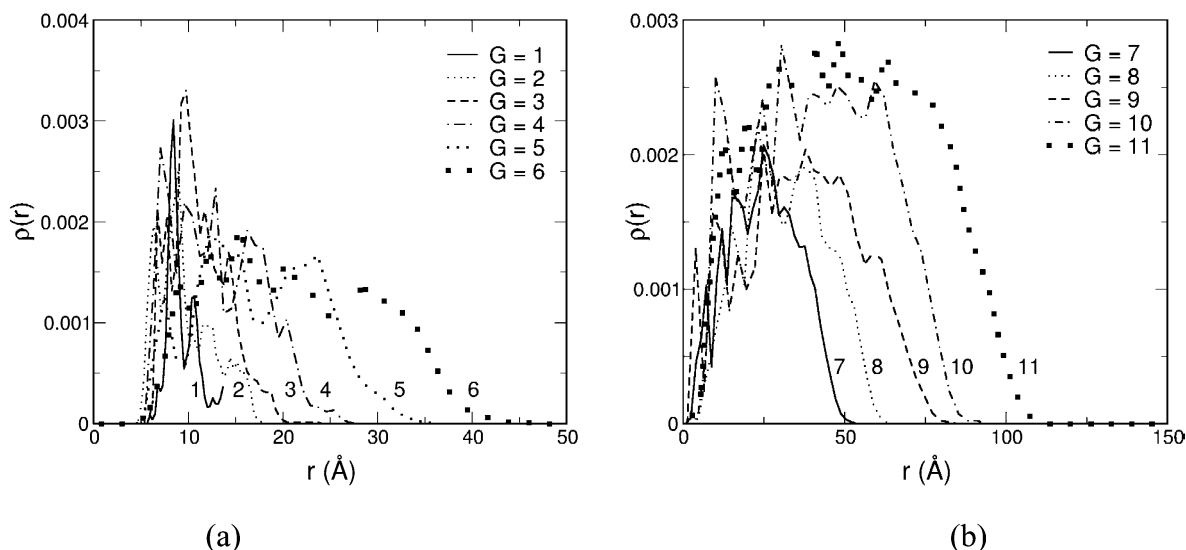
Figure 7. Radial densities for the terminal nitrogens (primary amines) for various generations of PAMAM dendrimer. Our values were averaged from snapshots every 0.5 ps in the dynamics (after equilibration).

systems.[55] We find that the nitrogen distribution has a peak near the periphery of the dendrimer and decays quickly beyond this distance. However, it shows an appreciable probability density within the interior region of the dendrimer. Also we see that the density distribution is multimodal, indicating that the terminal nitrogens make clusters and reside in a shell-like structure. Multimodal distribution of the end groups was also reported in the recent MD studies in PPI dendrimer.[25]

Figure 8 shows the spatial distributions of primary and tertiary nitrogens for a central slab of 8 Å thickness passing through the center of the molecule. This is shown for the final snapshot of the trajectory for generations 6 and 11. We see that primary nitrogens are distributed throughout the molecule, penetrating to the core in each molecule. For the higher generations, we find a larger number of primary and the outer generation tertiary nitrogens crowded into the core. Recently, Rosenfeldt et al.[10] reported SANS experiments in which labeled solutions of generation 4 poly(propylene amine) (PPI) dendrimers were examined in protonated and deuterated dimethylacetamide. They found similar evidence, indicating the presence of back-folding.

However from SANS experiments on dilute solutions of G7 PAMAM dendrimers, Topp et al.[56] concluded that back-folding is insignificant for PAMAM dendrimers in methanol and its deuterated form CD_3OD. They based this conclusion on the increase in the R_g for deuterated samples. From SANS with deuterium labeling and scattering contrast variation they found $R_g = 39.3 \pm 1$ Å for G7 terminal groups only and found $R_g = 34.4 \pm 0.2$ Å for the full dendrimer. This led them to conclude that the terminal groups are located at the outer surface of the dendrimer. To compare our simulation results with the SANS experiment, Table 2 tabulates the radius of gyration R_N considering only the location of the primary nitrogens (terminal groups). For G7 PAMAM, we find $R_g = 29.5 \pm 0.2$ Å and $R_N = 32.1 \pm 0.4$ Å. Thus, the theory leads to a ratio of $R_g/R_N = 0.91 \pm 0.03$, which can be compared to the experimental ratio of 0.88 ± 0.03. Thus, within the experimental uncertainty, the ratio obtained from our simulation is same as that obtained in the experiment, yet in our simulation, we find that the terminal groups (primary amines) are

distributed through the interior of the G7 PAMAM dendrimer. Our findings are consistent with the results from the recent Brownian dynamics simulation by Lyulin et al.[57,58] where they have shown that the radii of gyration are not always a safe measure of the location of the terminal groups and distribution functions with $R_N \geq R_g$ can be achieved even when most of the end groups are located within the interior of the dendrimer molecules

Assuming a perfect spherical shape and uniform density, the effective size of the dendrimer is $R = \sqrt{5/3} R_g = 38.13$ Å for G7 dendrimer (see Table 4) which is larger than R_N by 6 Å. This indicates how much the terminal groups are back-folded into the interior portion of the dendrimer. This is also evident from the density profile for the primary nitrogens.

One caveat in comparing theory and experiment is that our simulations are performed in a vacuum, corresponding to poor solvent conditions, whereas the experiments are performed in methanol. We find that the protonated and deuterated samples in a polar solvent (water) swell by 20% in explicit solvent MD calculations on G6 [30] PAMAM dendrimers as compared to the vacuum.

3.5. Branch Point Distribution. There is controversy as to how the different branches ("spacers") of the dendrimer arrange in space as we go radially outward form the center of mass of the dendrimer or as the generation increases. Do they arrange, in a regular fashion, as so often characterized in publications? The overall shape of the dendrimer may also dependent on the arrangements of various branches within the molecule. To understand how the spacer and branch point arrange spatially, we computed the angle between the vectors joining the branch points as a function of branch point generations. These angles are calculated from the scalar products $\langle I_m \cdot I_{m+1} \rangle$ where I_m and I_{m+1} are the two vectors joining different generation branch point from the center of the core (Figure 9). For G6–G8, Figure 10 shows that the angle is ~25° for G1–G4 and then decreases as m increases. On the other hand, for G10 and G11 we find that the angle increases dramatically from 12° for G1 to 45° for G4 and then gradually decreases for larger generations. This implies that the
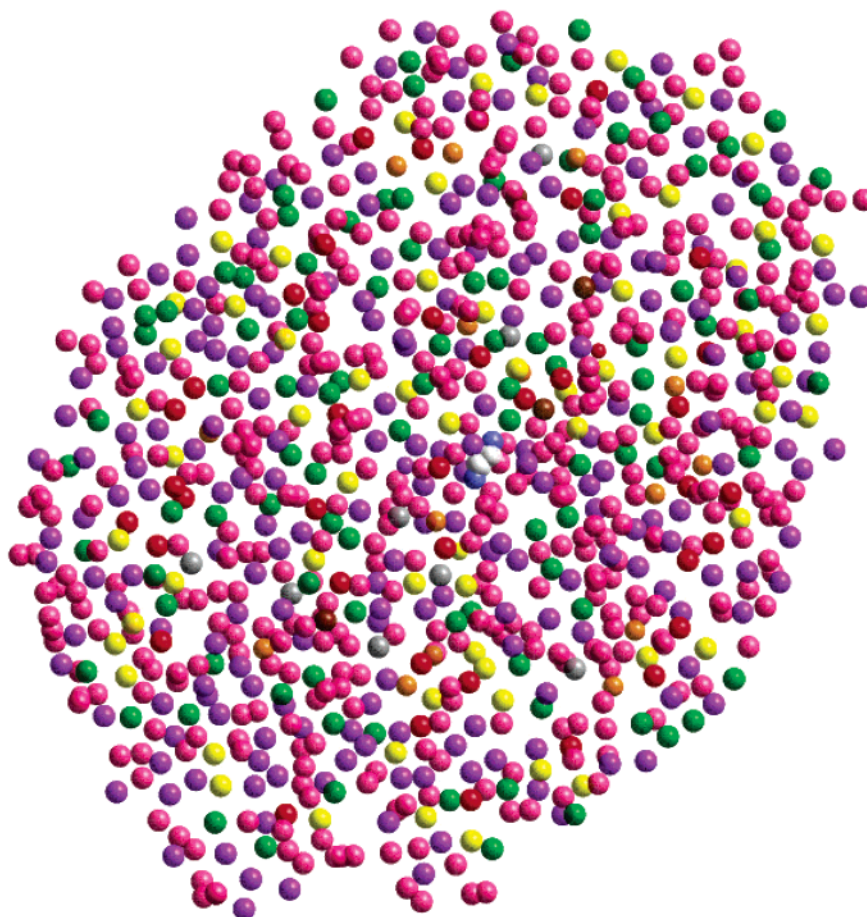
Figure 8. Instantaneous snapshots showing spatial arrangements of the primary and tertiary nitrogens for G6 and G11 PAMAM dendrimer in a slice of thickness 8 Å passing through the center of mass (white spheres) and in the *xy* planes. White spheres indicate to the center of the molecule. For G6, the primary nitrogens are magenta, the tertiary nitrogens of G5 are dark gray, and the tertiary nitrogens of G4 are green. For G11 the primary nitrogens are magenta, the tertiary nitrogens of G10 are dark gray, the tertiary nitrogens of G9 are green, the tertiary nitrogens of G8 are yellow, and the tertiary nitrogens of G7 are red. The magenta spheres (primary nitrogens) penetrate to the core of the molecule.
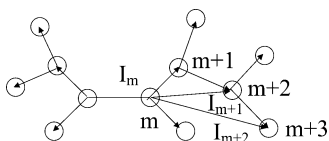
Figure 9. Definition of branch point and vectors joining them: I_m, I_{m+1}, ..., etc. Each of the branch points corresponds to the location of the primary or tertiary nitrogen.

core is very stretched for G10 and G11. G5 seems to have anomalous behavior.

A second analysis giving a similar conclusion is the branch point distance from center of core of the dendrimer as a function of branch point generations in Figure 11. Figure 11b shows that for G3–G6, the distance between successive branches oscillates around 4–8 Å, with an average of 6 Å. Then for G7–G9 the branch point distances for inner two subgenerations (g1 and g2) increase to 9–10 Å but decrease for the later layers. However, for G10, the distance of the first branch point from the core increases to 14 Å while that of the second branch point is 11 Å. For G11, we see dramatic increase in the distance of the first branch point (almost
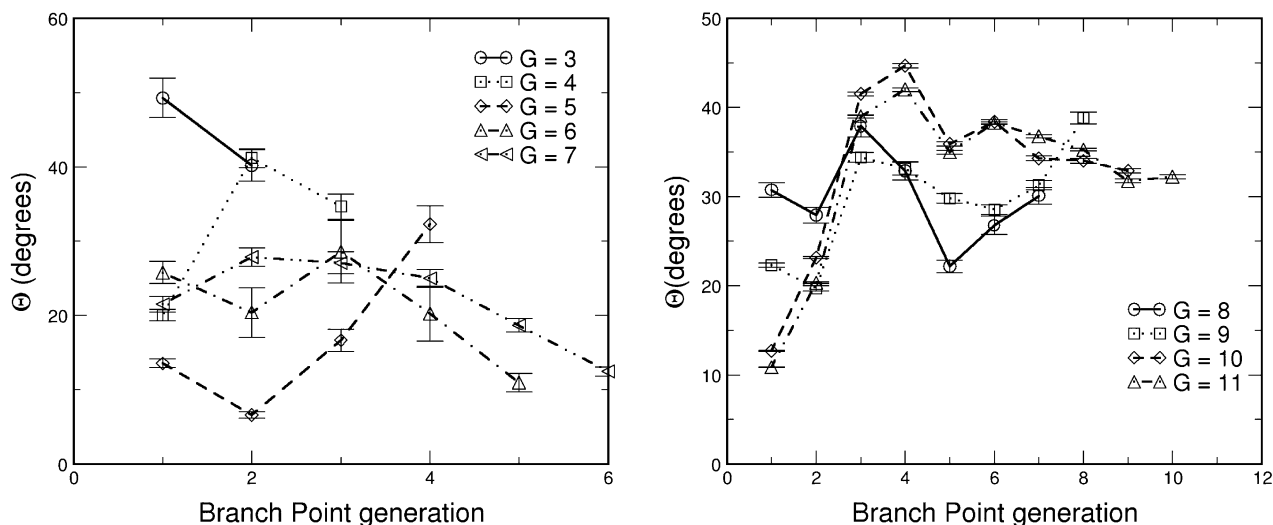
Figure 10. Angle between adjacent branch points as a function of branch point generation for various generations PAMAM dendrimer. The angle is defined as the dot product between the vectors $\bar{I}_m$ and $\bar{I}_{m+1}$. Lines are guide only to the eye.

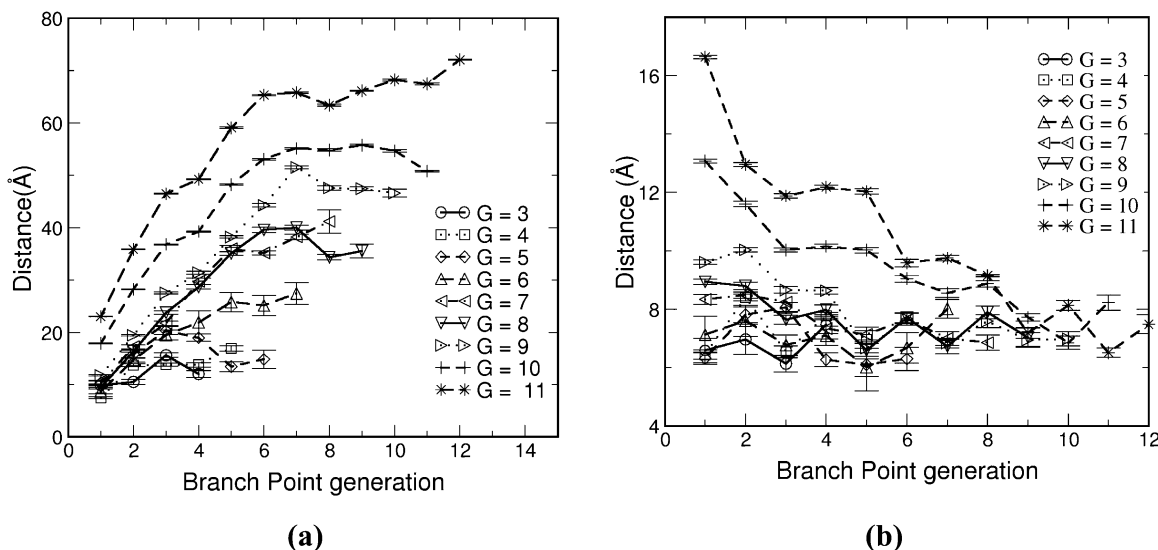**(a)**   **(b)**

Figure 11. Branch point distance distributions functions: (a) distance measured from the center of core to the branch point for different generation PAMAM dendrimer; (b) distance measured between consecutive branch points as a function of various generation PAMAM dendrimer.

17 Å) while the second branch point extends up to 14 Å. Then for G3–G5, the branch points are spaced by 10 Å for G10 and 12 Å for G11. Finally, by the outer two layers, the branch point distances are down to normal values of 6–8 Å, just as for smaller generations. This indicates that for G10 and even more in G11, addition of the outer layers has greatly stretched the inner layers with the effects magnified for the innermost three layers.

These results are consistent with our earlier observation that the core domain is denser for G1–G3 compared to the generations >G4. This picture indicates that the dendrimer is less dense in the interior for lower generation and extends out from the core. From the density profiles for various generations we also see that the monomer density is maximal at the core and decays radially outward for G1–G3.

This enormous strain in the inner region is even more manifest in an instantaneous snapshot (see Supporting Information) of the core and inner 2 subgenerations for G6 and G11 PAMAM dendrimer. This shows that the core of G 11 is stretched by a factor of 2 compared to G6.

This distribution of strains in the core region is in contrast to the picture of de Gennes and Hervet [13] in which the spacers closer to the core were expected to be less extended than the ones near the periphery. We interpret this opposite result as arising because stretching the core generations provides a larger radius giving space for the monomers belonging to the back-folded higher generations which thereby avoids steric congestion.

3.6. Solvent Accessible Molecular Surface and Volume. The interaction of the dendrimer with the solvent is largely determined by its solvent accessible surface area (SASA) and solvent excluded volume. PAMAM dendrimers have a great deal of internal surface area and solvent accessible volume as demonstrated by earlier studies[1] on NH_3-cored PAMAM dendrimers from generation 0 through 6.

To calculate the solvent accessible surface area A_{SASA} and volume A_{SAV}, we assume a fused-sphere model for the solute in which each sphere has a radius r_i equal to the van der Waals radius of the atom it represents, r_i^{vdW}, but extended by the probe radius of the solute, r_p. Thus, $r_i = r_i^{vdW} + r_p$. Thus, we extend the radius of each atom
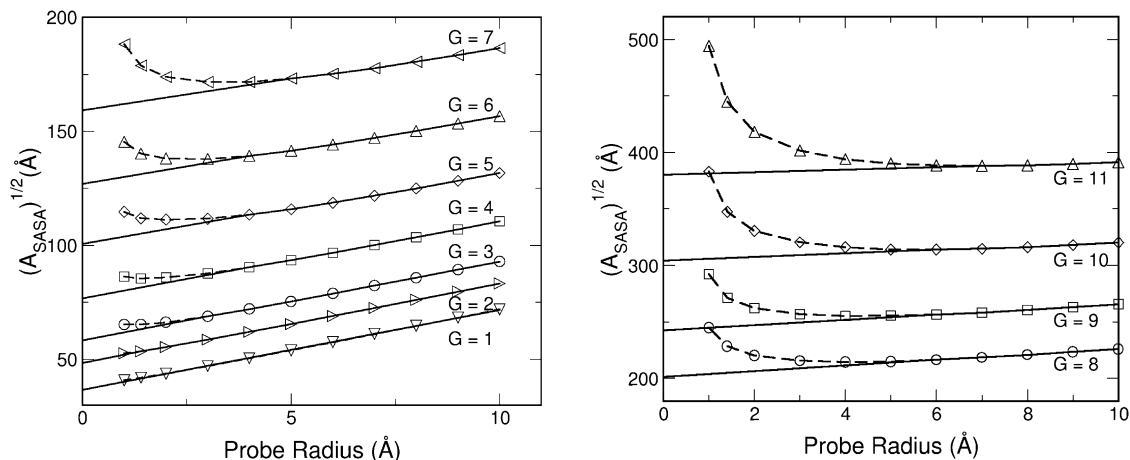
Figure 12. $\sqrt{A_{SASA}}$ as a function of probe radius for various generations PAMAM dendrimer. The line fitting larger probe radii extrapolated to zero probe radius provides a measure of the outside area (excluding pores and internal voids) while the difference between the calculated points and this line gives the internal area of the pores and internal voids.
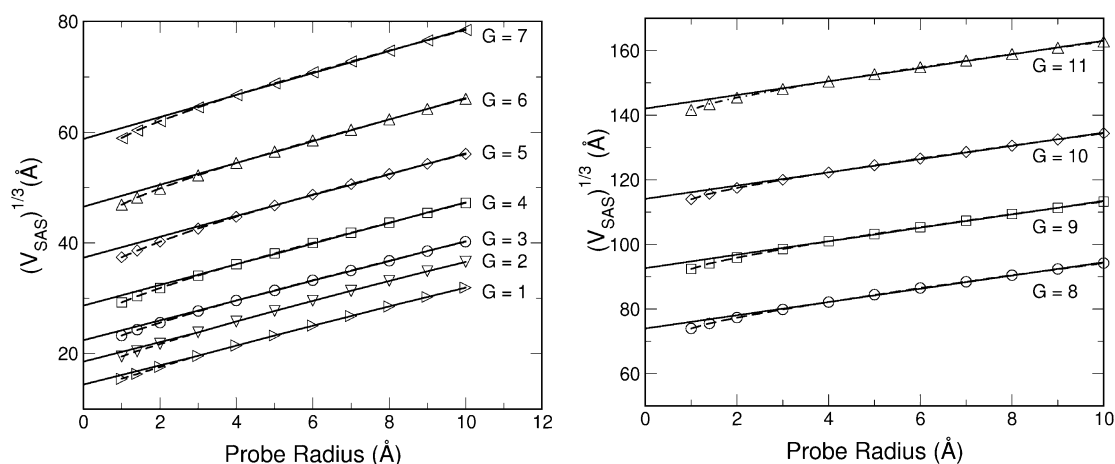

Figure 13. $V_{SAS}^{1/3}$ as a function of probe radius for various generations PAMAM dendrimer. The line fitting the larger probe radius extrapolated to zero probe radius provides a measure of the total volume (including pores and internal voids) while the difference between the calculated points and this line gives the internal volume of the pores and internal voids.

by the probe radius, leading to SASA as the surface area traced by the center of a spherical solvent probe as it rolls around the van der Waals surfaces of the solute. To calculate A_{SASA} and V_{SAS}, we have used the analytical volume generalized Born method (AVGB) developed in the Goddard group.[59] AVGB is very fast and accurate and has been applied successfully to study solvation effects in biological systems.[60]

3.6.1. Solvent Accessible Surface. Figure 12 plots $\sqrt{A_{SASA}}$ as a function of probe radius for different generation PAMAM dendrimers. For probe radii larger than the largest internal void, the SASA increases linearly with the probe radius. Fitting a line to these larger probe radii results and extrapolating to zero probe radius provide a measure of the surface area on the outside of the dendrimer (excluding pores and internal voids). Assuming the shape of the dendrimer to be a sphere, this exterior surface area leads to an estimate of the radius of the dendrimer, which is included in figure 17 and Table 4. This value is about 15−21% larger than our best estimate of the size.

The difference between the calculated points and the line in Figure 12 gives the internal area of the pores and internal voids. This internal surface area is plotted as a function of generation for several probe radii (1, 1.4, 2, and 3 Å) in Figure 14 a. This shows that, starting at generation 7, there is more internal surface area than

the external surface and the available internal surface area increases with higher generations.

3.6.2. Solvent Accessible Volume. The volume associated with the internal cavities can be obtained by calculating the volume contained inside the SASA, which is called the solvent accessible volume (V_{SAS}) as a function of probe radius. For a prefect sphere devoid of internal cavities, the volume contained within the sphere's SASA is given by

$$V_{SAS} = (4\pi/3)(R + p)^3 \qquad (9)$$

Figure 13 plots $3\sqrt{V_{SAS}}$ as a function of probe radius p for different generations PAMAM dendrimer. For larger probe radius $3\sqrt{V_{SAS}}$ is linear in p with a slope $3\sqrt{4\pi/3}$. The intercept at zero probe radius leads to an estimate of the volume contained inside the dendrimer, including all internal pores and cavities.

Using the limit of the line in Figure 13 for $p = 0$ leads to an estimate of the size R of the dendrimer in Table 4 and plotted in Figure 17 as a function of dendrimer generation. This value is in excellent agreement with the value obtained from the R_g, which Figure 3 shows is in good agreement with experiment.

The deviation of the V_{SAS} from the line in Figure 13 gives a measure of the volume contained in the internal
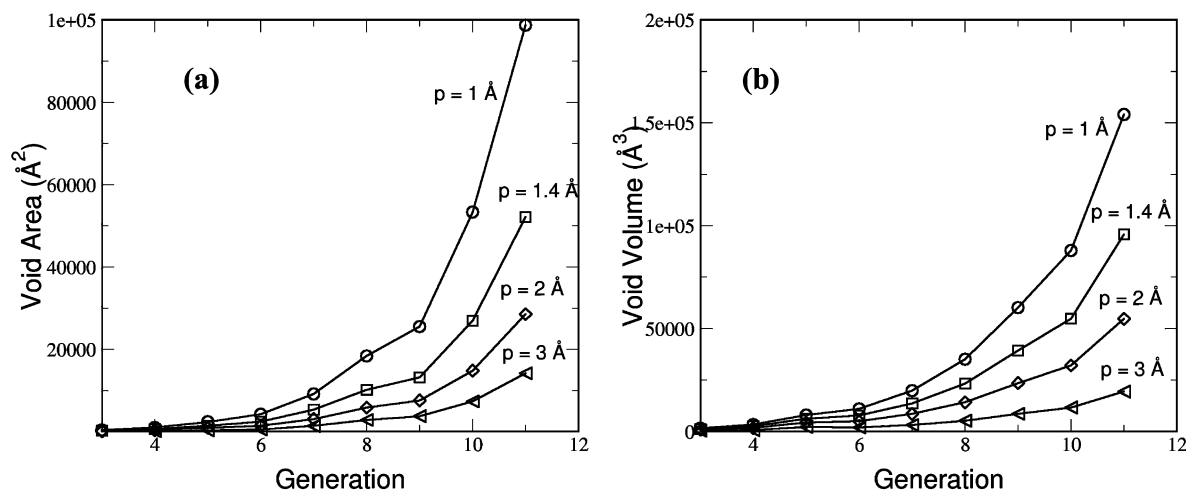
Figure 14. Internal surface area (S_{int}) (a) and volume (V_{int}) (b) plotted as a function of generation for several probe radiuses. The area and volume has been calculated from the difference between the points and lines in Figures 12 and 13.

Table 4. Sizes of the Various Generation PAMAM Dendrimers Computed Using Four Different Procedures as Discussed in the Text[a]

generation	R_{SASA} (Å)	R_{SAV} (Å)	R (Å) calcd from eq 10	R_N (Å)
1	10.33	8.95	9.63	10.35
2	13.63	11.49	11.84	11.61
3	16.43	13.91	14.72	12.91
4	21.35	17.77	18.69	16.81
5	28.38	23.15	24.11	20.26
6	35.79	28.87	31.26	25.94
7	44.93	36.44	38.13	31.55
8	56.79	45.90	47.62	39.87
9	68.37	57.45	60.29	47.94
10	85.72	70.80	70.54	57.38
11	107.23	88.12	88.12	70.86

[a] The size obtained from $R = R_g/\sqrt{3/5}$ agrees with R_{SAV} obtained from the volume contained within the solvent accessible volume (V_{SAS}), which we consider the best size measure. Note that the average radius of the outer generation nitrogens is consistently 20% smaller.
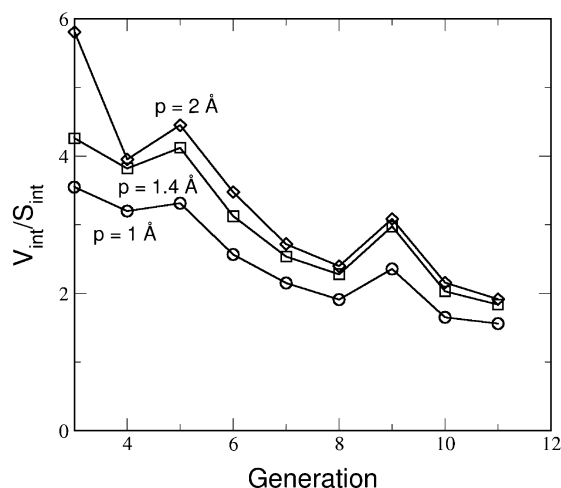

Figure 15. Internal surface area (S_{int}) (a) and volume (V_{int}) (b) plotted as a function of generation for several probe radiuses. The area and volume has been calculated from the difference between the points and lines in Figures 12 and 13.

voids and cavities. This internal void volume is plotted as a function of generation for several probe radii (1, 1.4, 2, and 3 Å) in Figure 14b. This shows that, starting at generation 7, there is an increase in the internal volume.

3.6.3. Analysis of the Character of Internal Voids and Pores. The measures of internal surface area and internal volume in Figure 14, parts a and b, can be used to estimate the character of the internal voids. Assuming that these voids consist of N_{int} equal sized spheres of radius R_{int} leads to an estimated size of $V_{int}/S_{int} = R_{int}/3$ and $N_{int} = S_{int}/4\pi R_{int}^2$. On the other hand, assuming that there is a single continuous pore of cylindrical shape of radius R_{int} and length d_{int} leads to $V_{int}/S_{int} = R_{int}/2$ and with $d_{int} = S_{int}/2\pi R_{int}$. Figure 15 shows V_{int}/S_{int} as a function of generation. This shows the radius distribution of voids as a function of generation.

These results can be compared to the internal structure of the various generations of dendrimer in Figure 16. This shows the solvent excluded surface area for a slice 2 Å thick passing through the center of each PAMAM dendrimer for G3–G11. From these cross-sections, we see that core is very dense compared to the exterior regions up to G6, but starting at G9, we see increasing numbers of voids and channels within the dendrimer. Most of the voids and cavities are located at the periphery of the dendrimer. The voids inside the dendrimer are filled by back-folding of the outer sub-generations throughout the interior of the molecules.

For some applications of dendrimers, it is valuable to have internal cavities and channels where that can accommodate specific molecular guests. Thus, Naylor and Goddard[16] showed that dopamine fitted well within a G6 NH3-cored PAMAM dendrimer. These internal voids can be controlled by the monomers from which the dendrimer is constructed (which may change as a function of growth generation) or by changing the character of the terminal generation. Thus, terminal groups that form favorable hydrogen bonds or electrostatic interactions with the polar solvents might reduce the degree of back-folding leading to the additional internal cavities and more internal space. Similarly this might be achieved by making the terminal groups repel each other. However, as mentioned earlier the conformations of the dendrimers of the higher generations are less flexible making them less sensitive to the presence of polar solvent or protonation of the terminal groups. This suggests that higher generations PAMAM dendrimer will form fewer internal voids and cavities.

3.7. Size of Dendrimers from Surface, Molecular Volume, and R_g Calculations. Assuming a uniform
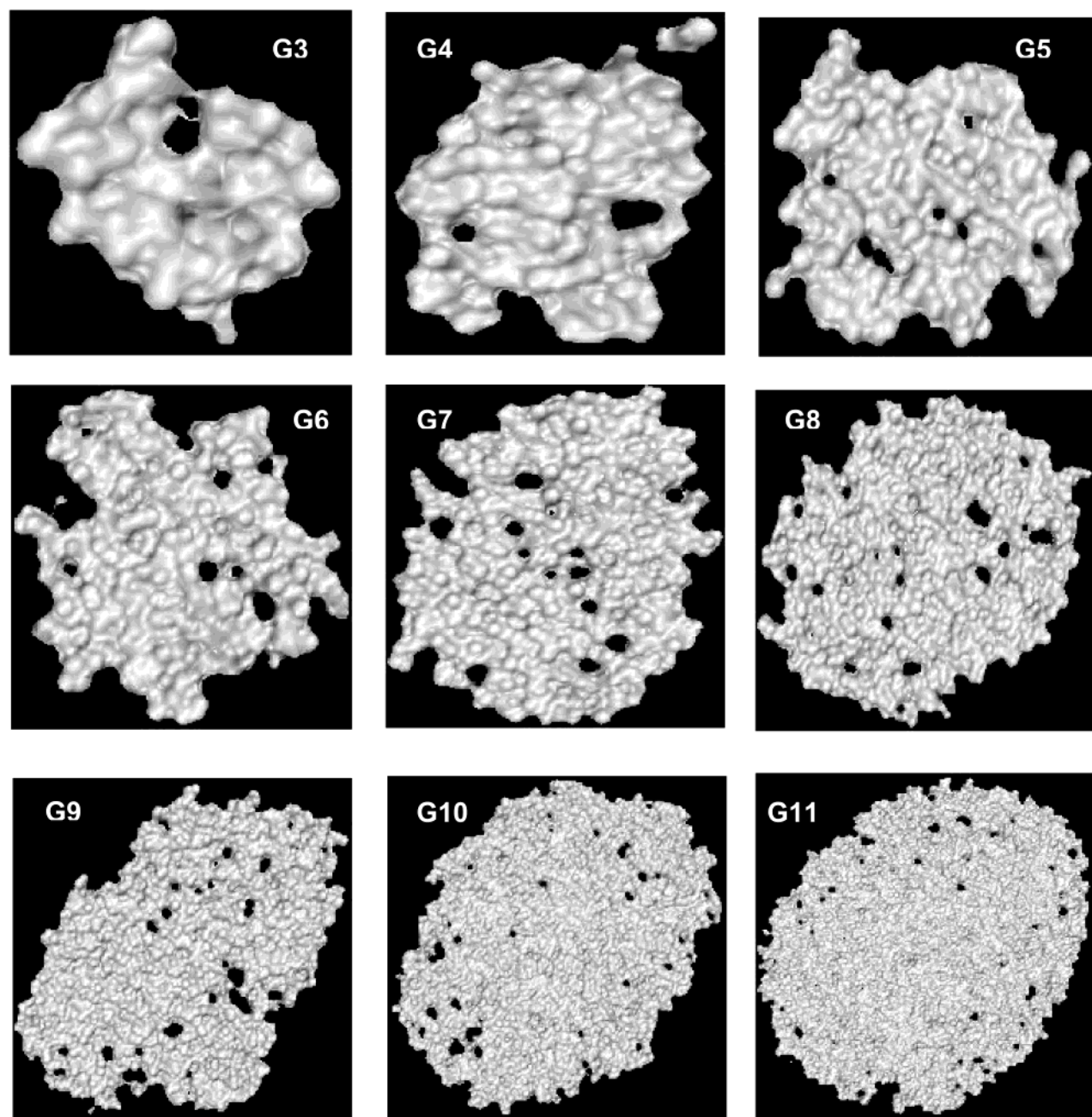
Figure 16. Solvent excluded surface area for generations 3−11 EDA-cored PAMAM dendrimer. To see the interior structure we show *xy* cuts from the middle of the dendrimer. These figures were generated using the MSMS package[62] from Scripps.

sphere, the radius of the dendrimer R is related to the radius of gyration of the dendrimer R_g via

$$R = R_g/\sqrt{3/5} \qquad (10)$$

As discussed above, Figures 12 and 13 lead to an estimated radius (assuming a spherical shape). Figure 17 and Table 4 compare the dendrimer radius from these three different methods. We also show here the radius of the dendrimer R_N obtained by computing the radius of gyration using only the primary nitrogens.

Starting with G2, the value of R_N is systematically smaller than the size obtained from R_g and R_{SAV} due to back-folding of the primary nitrogens within the dendrimer. This is more pronounced at higher generations since the degree of back-folding increases at higher generations. On the other hand the R_{SASA} value is

consistently larger. The R_{SAV} value is close to the R_g value, which is shown in Figure 4 to be close to experimental measures.

3.8. Fractal Dimension. Molecular surfaces play an important role in determining the structure and interactions properties of dendrimer molecules. They also play an important role in understanding the origin of specificity and recognition in the molecular interactions. Figure 18 shows the variation of the molecular surface area A_{mol} as a function of the probe radius, R_p. From this plot, we can extract the fractal dimension of the dendrimer using the following relation

$$2 - d_f = \frac{d(\log(A_{mol}))}{d(\log(R_p))} \qquad (11)$$

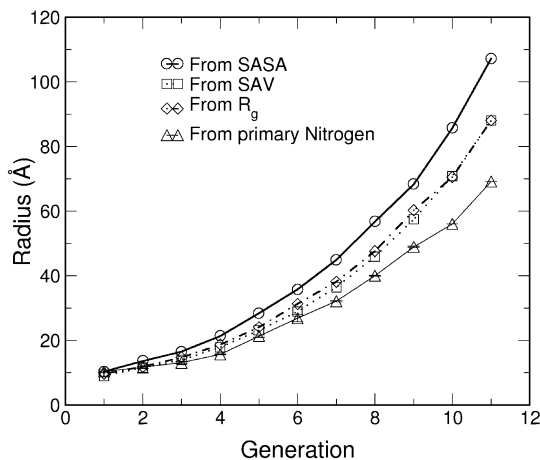where d_f is the fractal dimension of the dendrimer.

Figure 17. Comparison between the sizes of dendrimer calculated by four different methods. The size obtained from $R = R_g/\sqrt{3/5}$ agrees with R_{SAV} obtained from the volume contained within the solvent accessible volume (V_{SAS}), which we consider the best size measure. Note that the average radius of the outer generation nitrogens is consistently 20% smaller.
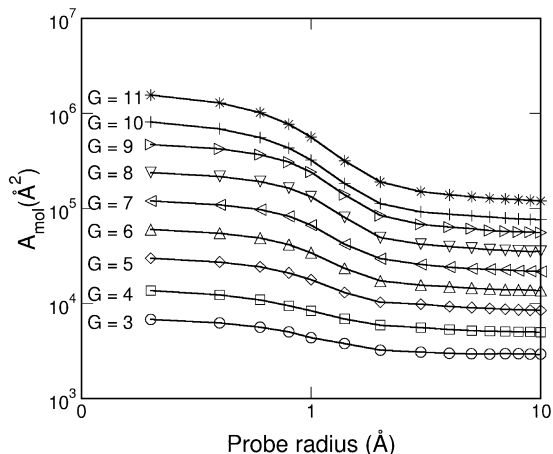

Figure 18. Molecular surface are A_{mol} plotted as a function of probe radius for different generations dendrimers in a log–log scale. As discussed in section 3.6, the fractal dimension of the external surface is $D = 3.6$ for G11 and $D = 2.5$ for G3. A perfectly smooth spherical surface leads to $D = 3$, indicating the nonsphericity for G3 and the tortuous outer surface for G11.

Figure 18 shows that at both small and large probe radius, the slope of the curves for different generation is almost zero, indicating $d_f = 3$. However, for probe radius in the intermediate range (1−4 Å) the fractal dimension increases from 2.5 for G3 to 3.57 for G11. The average fractal dimension d_f is 3.1. Since the fractal dimension of an object in Euclidian space is limited by the dimensionality of the space, we consider the fractal dimension of our model dendrimers to be $d_f = 3.0$ within the accuracy of the simulation data. This means that these dendrimers are very dense and completely space-filling objects. The fractal dimension for G9 and above are significantly larger than 3. We consider that this indicates a very irregular surface, leading more surface area than expected from its radius. This is also shown in Figure 18, where the radius derived from the surface area is too large compared to other measures.

Murat and Grest,[26] using a bead model in Brownian dynamics simulation, obtained a fractal dimension of 3.0 in good agreement with ours. On the other hand, Mansfield[21] using Monte Carlo simulation on diamond
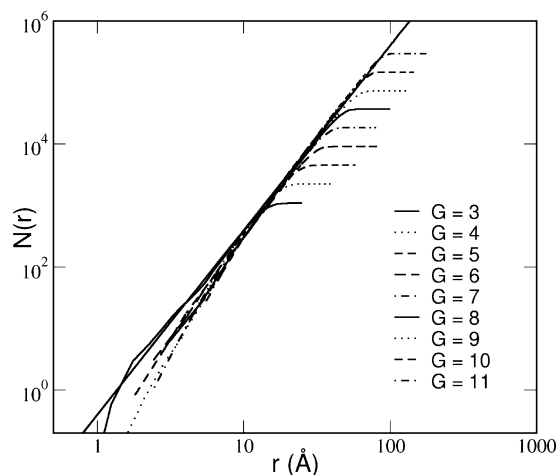

Figure 19. A log−log plot of number of monomers $N(r)$ that reside within a sphere of radius r for different generation dendrimers. The solid line has the form $N(r) = 0.4r^3$, which indicates that different generations dendrimers have the same fractal dimension $d_f \approx 3.0$.

lattice calculated the fractal dimension using the box method, obtained a lower value, $d_f = 2.79$ for G9. To determine the origin of this discrepancy, we also estimated the fractal dimension of the dendrimer in a manner similar to the box method. In this method, we plot the number of monomers $N(r)$ within a sphere of radius r from the center of mass of the dendrimer.[26] Figure 19 shows the variation of $N(r)$ as a function of r. From the best power law fits to the curves we find that the fractal dimension is $d_f = 3.0$, which is the same as the value obtained from plotting molecular surface area. Thus, we are not sure why the Mansfield number is different.

4. Structure Factor

One of the few experimental ways to characterize the structure of dendrimers is with SANS or SAXS, which gives a measure of the overall size. Closely related to the results of SANS or SAXS experiments is the spherically averaged Fourier transform of the single particle density, $S(q)$, given by eq 12[21]

$$S(q) = \frac{1}{4\pi N^2}\int_0^{2\pi} d\phi \int_0^{\pi} \sin\theta \, d\theta \, |\sum_{i=1}^{N} \exp[i\vec{q}.\vec{r}_j]|^2 \quad (12)$$

where

$$\vec{q} = q\sin\theta\cos\phi\hat{x} + q\sin\theta\sin\phi\hat{y} + q\cos\theta\hat{z} \quad (13)$$

We calculated this using orientation averaging at intervals of 9° in both θ (0< θ < 180°) and φ (0< φ < 360°). Since there is no strong conformational change in the dendrimer structures over the dynamics, the averaging has been done for 20−30 configurations spread uniformly over the 200 ps of dynamics up to generation 8 and for 10 configurations spread uniformly over the 50−100 ps of dynamics for generations 9−11. Figure 20a plots the single particle form factor for G1−11 PAMAM dendrimers in the Kratky representations. The Kratky representation makes the function independent of size. Thus, particles uniformly distributed in a sphere would lead to the shape independent of the generation. This allows us to study the structure of various generation dendrimers in a length indepen-
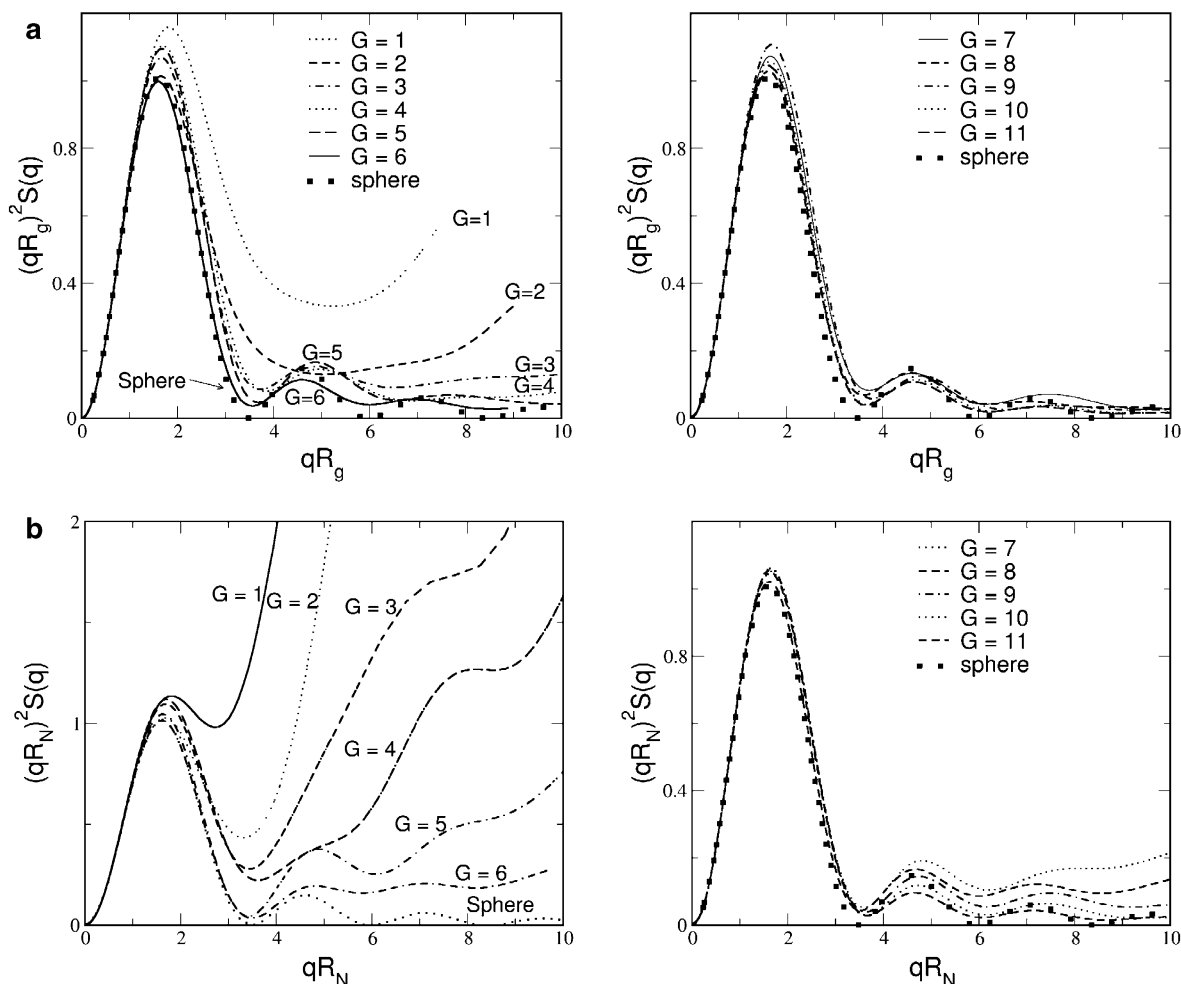
Figure 20. (a) $S(q)$, the single particle form factor (Fourier transform of the single particle density, (eq 12) for PAMAM dendrimers for generations 1–11. We use Kratky representation, which makes the function independent of size. Particles uniformly distributed in a sphere would lead to the dashed line. This indicates that G1 and G2 are very far from spherical while G6 and above are quite spherical. (b) Single particle form factor in Kratky representation for PAMAM dendrimers for generations 1–11. R_N is the radius of gyration of the dendrimer considering the locations of the terminal nitrogens only.

dent way and highlights any differences in their density distributions. For comparison we also show the results for a sphere of radius 30 Å which is close to the size of $G = 6$ PAMAM dendrimer. For $G = 3$ and higher, the first major peak appears at $1.66 \geq qR_g \geq 1.62$, which compares very well with the value of $qR_g \sim 1.63$ for the perfect sphere. For lower generations (G1 and G2), the peak occurs at $qR_g \sim 1.79$ for $G = 1$ and at $qR_g \sim 1.65$. This indicates that G1 and G2 are very far from spherical while G6 and above are quite spherical. The appearance of distinct peaks for higher generations (>G3) in the range $4 < qR_g < 10$ indicates that higher generation dendrimers have very well-defined shapes, becoming more spherical in shape for higher generations. Apart from G1 and G2, all generations have similar shapes in the scattering curves and look similar to the SAXS scattering curves reported by Prosa et al.[61] (see Figure 7 in this reference).

We also calculated $S(q)$ by considering the distribution of terminal nitrogens only. This is plotted in Figure 20b using the Kratky presentation. R_N is the radius of gyration taking into consideration the location of primary nitrogens only. Here also we see that at higher generations the distribution of primary nitrogens becomes more spherical. A detailed comparison of the form factor obtained from our simulations with those ob-

tained from recent SAXS experiment will be presented elsewhere.

5. Quest for the Limiting Generation

The number of monomer in a given generations grows as

$$N = C_{\text{core}} + c \sum_{g=1}^{g_{\text{max}}} m^{g-1} M \tag{14}$$

where C_{core} is the number of monomers in the core region, c is the number of branches of the core, and m is the multiplicity of monomer. For EDA-cored PAMAM, $C_{\text{core}} = 8$, $c = 4$, and $m = 2$, while $M = 17$ for inner generations and 19 for the terminal generation. Since the number of atoms increases exponentially with generation number while the available surface area increases slowly, we expect steric overlap between surface terminal groups to limit the maximum generation that can be completed chemically. For higher generations starburst dendrimers must become imperfect. This argument that there is a limiting generation was first raised by de Gennes and Hervet.[13] Assuming a Flory–Huggins analysis for the entropy of mixing and assuming that each branch is a freely joined chain with
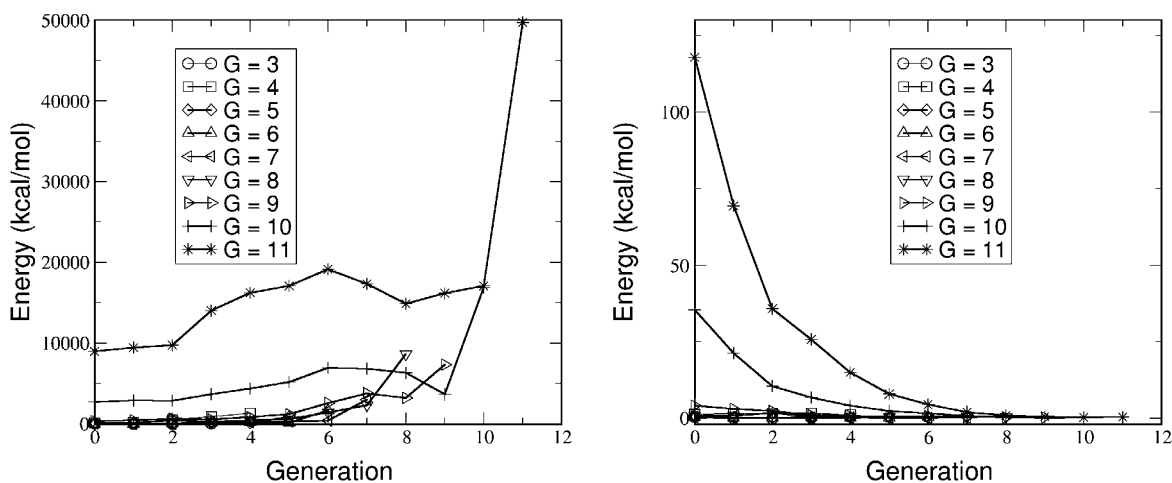
Figure 21. Total energy of the monomers belonging to each subgenerations for various generations of PAMAM dendrimers. This shows that up to G6 there is very little strain anywhere and that G7 and G8 have additional strain only in the other generations. However, with G11 there is a great deal of strain throughout the system, while G10 also has strain throughout the system. (b) Energy per monomer belonging to various subgenerations. Starting from $G = 10$, the strain energy per monomer becomes very large, indicating that that the growth might be prohibited somewhere between $G = 10$ and $G = 11$.

length Pa (a is the bond length which is the distance between the two spacer points), de Gennes and Hervet predicted the following relationship between the limiting generation g_{max} and number of spacers P

$$g_{max} = 2.88 \ln P + 4.4 \pm 0.2 \qquad (15)$$

Using $P = 7$ for the PAMAM dendrimer, this leads to $g_{max} = 10.2$. There has not yet been a theoretical or computational study to address this issue of limiting generations and test the de Gennes prediction.

To determine at which generation the growth would terminate, we consider the variation of strain energy (energy per monomer) as a function of generation. This is calculated by partitioning every term in the potential energy among the atoms involved. Thus, two-body interactions are half given to each atom, three-body interactions are associated with the central atom, torsional terms are half given to each internal atom, and inversions are attributed to the central atoms. Figure 21, plots the strain energy for monomers belonging to various subgenerations for various generations dendrimer. We see that for G10 and G11 the strain energy increases dramatically for the all subgenerations. In particular, G11 has a great deal of strain in both inner and outer subgenerations. This suggests that generation 11 is already past the limiting generation for the EDA-cored PAMAM dendrimer. Indeed, on the basis of the strain distributed throughout the structure, we suspect that normal synthesis techniques may not be able to complete G10, making it the limiting generation. These predictions that G10 is probably the limiting generation is also consistent with the prediction of 10.2 by de Gennes and Hervet.

As an alternative measure to determine the limiting generation, we consider the area available for each monomer as a function of generation. Using the R_{SASA} radius from Table 4, Figure 22 plotted the area available per terminal primary amine group. This area decreases monotonically from G1 to G11, until at G11 it is 17.6 Å^2 per monomer. To compare with this we calculated the SASA for a single primary amine group in CH$_3$NH$_2$ using a probe radius of 1.4 Å, leading to 28.4 Å^2 per NH$_2$ (horizontal line in Figure 22). Thus, the available area falls below this value between G10 and G11.
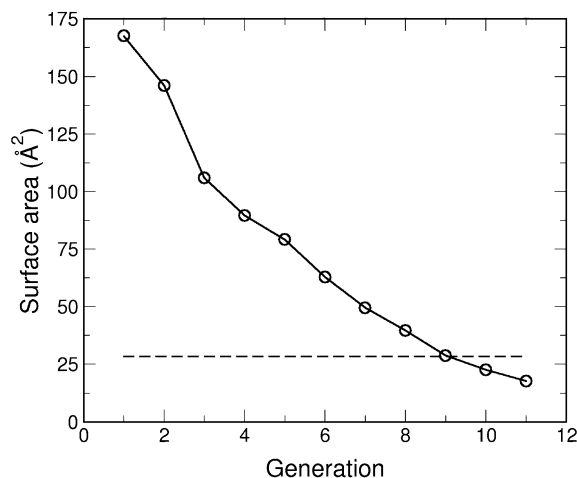

Figure 22. Available surface area per terminal amine group as a function of dendrimer generation. The solid line is a guide to the eye only. The horizontal dashed line represent the SASA for the NH$_2$ part of an isolated H$_3$C−NH$_2$ group.

6. Concluding Remarks/Summary

We report herein comprehensive atomistic MD study of PAMAM dendrimers over the entire range of generations (up to G11) for gas-phase conditions.

The calculated radius of gyration is in good agreement with SAXS and SANS experiments where available, leading to a size that scales accurately as $R \sim N^{1/3}$ for G3 to G11.

We find very little strain in these structures up to G6; however, for G10 there is significant strain throughout the entire structure, which increases dramatically for G11. This correlates with the surface area available per monomer, which is below the minimum required for G11. This strain causes considerable stretching of the inner two generations for G10 and G11. These results suggest that the steric interactions of the surface groups prevent growth of full generations beyond G10. This agrees with the predictions by de Gennes, which suggested a limit at $\sim$G10.2.

These simulations over the entire range up to the limiting generation clearly demonstrate the highly flexible nature of the PAMAM system, which leads to terminal groups being distributed throughout the inte-

rior of the dendrimer. This differs dramatically from the usual simplified 2D drawing.

These studies consider only gas phase (or poor solvent) conditions. Future work will examine the effect of polar solvents (e.g., H_2O) and protonation on the overall shape and size of various generations, but only up to ~G6.

Supporting Information Available: The .bgf files containing the *xyz* coordinates for a snapshot of the trajectory for each dendrimer from generation 3 to generation 11 in ascii format and a figure showing the monomer density profiles with respect to the center of core of the dendrimer. This material is available free of charge via the Internet at http://pubs.acs.org.

References and Notes

(1) Tomalia, D. A.; Naylor, A. M.; Goddard, W. A., III. *Angew. Chem., Int. Ed. Engl.* **1990**, *29*, 138−175.
(2) Tomalia, D. A.; Baker, H.; Dewald, J.; Hall, M.; Kallos, G.; Martin, S.; Roeck, J.; Ryder, J.; Smith, P. *Polym. J.* **1985**, *17*, 117−132.
(3) Tomalia, D. A. *Macromol. Symp.* **1996**, *101*, 243−255.
(4) Tomalia, D. A. *Adv. Mater.* **1994**, *6*, 529−539.
(5) Frechet, J. M. J. *Science* **1994**, *263*, 1710−1715.
(6) Hawker, C. J.; Frechet, J. M. J. *J. Am. Chem. Soc.* **1990**, *112*, 7638−7647.
(7) Hawker, C. J.; Wooley, K. L.; Frechet, J. M. J. *J. Chem. Soc., Perkins Trans,* **1993**, *12*, 1287−1297.
(8) Hawker, C. J.; Farrington, P. J.; Mackay, M. E.; Wooley, K. L.; Frechet, J. M. J. *J. Am. Chem. Soc.* **1995**, *117*, 4409−4410.
(9) Zimmerman, S. C.; Zeng, F. W.; Richert, D. E. C.; Kolotuchin, S. V. *Science* **1996**, *271*, 1095−1098.
(10) Rosenfeldt, S.; Dingenouts, N.; Ballauff, M.; Lindner, P.; Likos, C. N.; Werner, N.; Vogtle, F. *Macromol. Chem. Phys.* **2002**, *203*, 1995−2004.
(11) Topp, A.; Bauer, B. J.; Tomalia, D. A.; Amis, E. J. *Macromolecules* **1999**, *32*, 7232−7237.
(12) Prosa, T. J.; Bauer, B. J.; Amis, E. J. *Macromolecules* **2001**, *34*, 4897−4906.
(13) de Gennes, P. G. H.; H. *J. Phys. (Paris)* **1983**, *44,* L351.
(14) Naylor, A. M.; Goddard, W. A.; Keiffer, G. E.; Tomalia, D. A. *J. Am. Chem. Soc.* **1989**, *111*, 2339−2341.
(15) Bosman, A. W.; Janssen, H. M.; Meijer, E. W. *Chem. Rev.* **1999**, *99*, 1665−1688.
(16) Naylor, A. M.; Goddard, W. A., III. In *Biocatalysis and Biomimetics*; Burrington, J. D.; Clark, D. S., Eds.; ACS Symposium Series 392; American Chemical Society: Washington, DC, 1989; Chapter 6, pp 65−78.
(17) Lescanec, R. L.; Muthukumar, M. *Macromolecules* **1990**, *23*, 2280−2288.
(18) Welch, P.; Muthukumar, M. *Macromolecules* **1998**, *31*, 5892−5897.
(19) Welch, P.; Muthukumar, M. *Macromolecules* **2000**, *33*, 6159−6167.
(20) Mansfeld, M. L.; Jeong, M. *Macromolecules* **2002**, *35*, 9794−9798.
(21) Mansfield, M. L.; Klushin, L. I. *Macromolecules* **1993**, *26*, 4262−4268.
(22) Mansfield, M. L. *Polymer* **1994**, *35*, 1827.
(23) Mansfield, M. L. *Polymer* **1996**, *37*, 3835−3841.
(24) Mansfield, M. L. *Macromolecules* **2000**, *33*, 8043.
(25) Zacharopoulos, N.; Economou, L. G. *Macromolecules* **2002**, *35*, 1814−1821.
(26) Murat, M.; Grest, G. S. *Macromolecules* **1996**, *29*, 1278−1285.
(27) Rudnick, G.; Gaspari, G. *J. Phys. A* **1986**, *4*, L191.
(28) Sadanobu, J.; Goddard, W. A., III. *J. Chem. Phys.* **1997**, *106*, 6722.
(29) Sadanobu, J.; Goddard, W. A., III. *Fluid Phase Equilib.* **1998**, *144*, 415.
(30) Maiti, P. K.; Cagin, T.; Lin, S. T.; Goddard, W. A., III. To be published.
(31) Maiti, P. K.; Cagin, T.; Li, Y.; Goddard, W. A., III. To be published.
(32) Percec, V.; Ahn, C. H.; Ungar, G.; Yeardley, D. J. P.; Moller, M.; Sheiko, S. S. *Nature (London)* **1998**, *391*, 161−164.
(33) Hudson, S. D.; Jung, H. T.; Percec, V.; Cho, W. D.; Johansson, G.; Ungar, G.; Balagurusamy, V. S. K. *Science* **1997**, *278*, 449−452.
(34) Percec, V.; Chu, P. W.; Ungar, G.; Zhou, J. P. *J. Am. Chem. Soc.* **1995**, *117*, 11441−11454.
(35) Lin, S. T.; Jang, S. S., Cagin, T., Goddard, W. A., III. *J. Phys. Chem.*, in press.
(36) Cagin, T.; Wang, G. F.; Martin, R.; Breen, N.; Goddard, W. A., III. *Nanotechnology* **2000**, *11*, 77−84.
(37) Cagin, T.; Wang, G. F.; Martin, R.; Zamanakos, G.; Vaidehi, N.; Mainz, D. T.; Goddard, W. A., III. *Comput. Theor. Polym. Sci.* **2001**, *11*, 345−356.
(38) Miklis, P.; Cagin, T.; Goddard, W. A., III. *J. Am. Chem. Soc.* **1997**, *119*, 7458−7462.
(39) Mayo, S. L.; Olafson, B. D.; Goddard, W. A., III. *J. Phys. Chem.* **1990**, *94*, 8897−8909.
(40) Rappe, A. K.; Goddard, W. A., III. *J. Phys. Chem.* **1991**, *95*, 3358.
(41) Ding, H. Q.; Karasawa, N.; Goddard, W. A., III. *J. Chem. Phys.* **1992**, *97*, 4309.
(42) Lim, K. T.; Brunett, S.; Iotov, M.; McClurg, R. B.; Vaidehi, N.; Dasgupta, S.; Taylor, S.; Goddard, W. A., III. *J. Comput. Chem.* **1997**, *18*, 501−521.
(43) Nisato, G.; Ivkov, R.; Amis, E. J. *Macromolecules* **1999**, *32*, 5895−5900.
(44) Nisato, G.; Ivkov, R.; Amis, E. J. *Macromolecules* **2000**, *33*, 4172−4176.
(45) Evmenenko, G.; Bauer, B. J.; Kleppinger, R.; Forier, B.; Dehaen, W.; Amis, E. J.; Mischenko, N.; Reynaers, H. *Macromol. Chem. Phys.* **2001**, *202*, 891−899.
(46) Jackson, C. L.; Chanzy, H. D.; Booy, F. P.; Drake, B. J.; Tomalia, D. A.; Bauer, B. J.; Amis, E. J. *Macromolecules* **1998**, *31*, 6259−6265.
(47) Li, J.; Piehler, L. T.; Qin, D.; Baker, J. R.; Tomalia, D. A.; Meier, D. J. *Langmuir* **2000**, *16*, 5613−5616.
(48) Jockusch, S.; Ramirez, J.; Sanghvi, K.; Nociti, R.; Turro, N. J.; Tomalia, D. A. *Macromolecules* **1999**, *32*, 4419−4423.
(49) Karatasos, K.; Adolf, D. B.; Davies, G. R. *J. Chem. Phys.* **2001**, *115*, 5310−5318.
(50) Rapaport, D. C. *The art of molecular dynamics simulation*; Cambridge University Press: Cambridge, England, 1995.
(51) Humphrey, W.; Dalke, A.; Schulten, K. *J. Mol. Graph.* **1996**, *14*, 33-&.
(52) Boris, D.; Rubinstein, M. *Macromolecules* **1996**, *29*, 7251−7260.
(53) Wooley, K. L.; Klug, C. A.; Tasaki, K.; Schaefer, J. *J. Am. Chem. Soc.* **1997**, *119*, 53−58.
(54) Gorman, C. B.; Hager, M. W.; Parkhurst, B. L.; Smith, J. C. *Macromolecules* **1998**, *31*, 815−822.
(55) Gorman, C. B.; Smith, J. C. *Polymer* **2000**, *41*, 675−683.
(56) Topp, A.; Bauer, B. J.; Klimash, J. W.; Spindler, R.; Tomalia, D. A.; Amis, E. J. *Macromolecules* **1999**, *32*, 7226−7231.
(57) Lyulin, A. V.; Davies, G. R.; Adolf, D. B. *Macromolecules* **2000**, *33*, 6899−6900.
(58) Lyulin, A. V.; Davies, G. R.; Adolf, D. B. *Macromolecules* **2000**, *33*, 3294−3304.
(59) Zamanakos, G., A Fast and Accurate Analytical Method for the computation of Solvent Effects in Molecular Simulations. Ph.D. Thesis, Caltech, Pasadena, CA, 2002.
(60) Vaidehi, N.; Floriano, W. B.; Trabanino, R.; Hall, S. E.; Freddolino, P.; Choi, E. J.; Zamanakos, G.; Goddard, W. A., III. *Proc. Natl. Acad. Sci. U.S.A.* **2002**, *99*, 12622−12627.
(61) Prosa, T. J.; Bauer, B. J.; Amis, E. J.; Tomalia, D. A.; Scherrenberg, R. *J. Polym. Sci., Part B: Polym. Phys.* **1997**, *35*, 2913−2924.
(62) Sanner, M. F.; Olson, A. J.; Spehner, J. C. *Biopolymers* **1996**, *38*, 305−320.